



A high-resolution monitoring approach of urban CO₂ fluxes. Part 2 – surface flux optimisation using eddy covariance observations

Stavros Stagakis^{a,*}, Christian Feigenwinter^a, Roland Vogt^a, Dominik Brunner^b, Markus Kalberer^a

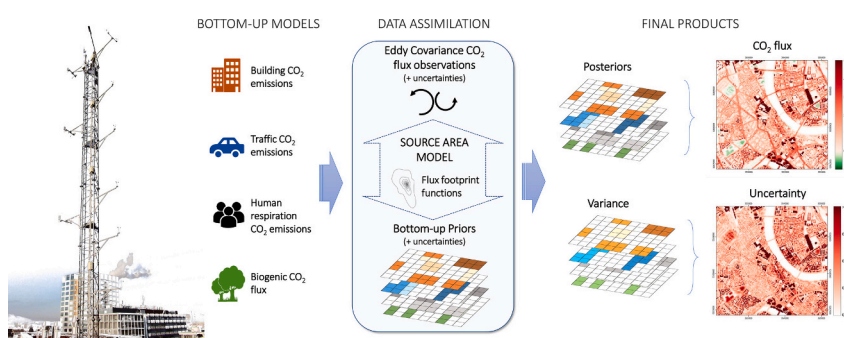
^a Department of Environmental Sciences, University of Basel, Klingelbergstrasse 27, 4056 Basel, Switzerland

^b Empa, Swiss Federal Laboratories for Materials Science and Technology, Überlandstrasse 129, 8600 Dübendorf, Switzerland

HIGHLIGHTS

- Urban CO₂ emission inventories need to be assessed using direct observations.
- Eddy covariance (EC) can provide direct urban CO₂ flux observations to inform models.
- A novel data assimilation approach between EC and bottom-up modelling is demonstrated.
- Each local CO₂ urban flux component is estimated at high spatiotemporal resolution.
- The method shows upscaling potential and complementarity to atmospheric inversions.

GRAPHICAL ABSTRACT



ARTICLE INFO

Editor: Anastasia Paschalidou

Keywords:

Carbon dioxide
Inversion modelling
Data assimilation
Source area modelling
Greenhouse gas
Climate change

ABSTRACT

Achieving climate neutrality by 2050 requires ground-breaking technological and methodological advancements in climate change mitigation planning and actions from local to regional scales. Monitoring the cities' CO₂ emissions with sufficient detail and accuracy is crucial for guiding sustainable urban transformation. Current methodologies for CO₂ emission inventories rely on bottom-up (BU) approaches which do not usually offer information on the spatial or temporal variability of the emissions and present substantial uncertainties. This study develops a novel approach which assimilates direct CO₂ flux observations from urban eddy covariance (EC) towers with very high spatiotemporal resolution information from an advanced urban BU surface flux model (Part 1 of this study, Stagakis et al., 2023) within a Bayesian inversion framework. The methodology is applied to the city centre of Basel, Switzerland (3 × 3 km domain), taking advantage of two long-term urban EC sites located 1.6 km apart. The data assimilation provides optimised gridded CO₂ flux information individually for each urban surface flux component (i.e. building heating emissions, commercial/industrial emissions, traffic emissions, human respiration emissions, biogenic net exchange) at 20 m resolution and weekly time-step. The results demonstrate that urban EC observations can be consistently used to improve high-resolution BU surface CO₂ flux model estimations, providing realistic seasonal variabilities of each flux component. Traffic emissions are determined with the greatest confidence among the five flux components during the inversions. The

* Corresponding author.

E-mail addresses: stavros.stagakis@unibas.ch (S. Stagakis), christian.feigenwinter@unibas.ch (C. Feigenwinter), roland.vogt@unibas.ch (R. Vogt), Dominik.Brunner@empa.ch (D. Brunner), markus.kalberer@unibas.ch (M. Kalberer).

<https://doi.org/10.1016/j.scitotenv.2023.166035>

Received 16 November 2022; Received in revised form 17 July 2023; Accepted 2 August 2023

Available online 3 August 2023

0048-9697/© 2023 The Authors. Published by Elsevier B.V. This is an open access article under the CC BY license (<http://creativecommons.org/licenses/by/4.0/>).

optimised annual anthropogenic emissions are 14.7 % lower than the prior estimate, the human respiration emissions have decreased by 12.1 %, while the biogenic components transformed from a weak sink to a weak source. The root-mean-square errors (RMSEs) of the weekly comparisons between EC observations and model outputs are consistently reduced. However, a slight underestimation of the total flux, especially in locations with complex CO₂ source/sink mixture, is still evident in the optimised fluxes.

1. Introduction

Cities, being responsible for around 70 % of the total fossil fuel CO₂ emissions globally (IPCC, 2022), are now facing an unprecedented challenge of reaching climate neutrality by 2050 (UNFCCC, 2015). To achieve this, climate change mitigation actions need to be planned and their effects must be monitored based on comprehensive and reliable quantitative information of urban emissions with sufficient spatial, temporal and functional detail (Hsu et al., 2019). To meet these needs, cities are developing local self-reported greenhouse gas (GHG) emission inventories based on bottom-up (BU) approaches (e.g. GCoM CRF, 2018; GHG Protocol, 2021). However, such inventories still do not provide sufficient spatial or temporal resolution to understand the urban function (Oke et al., 2017) and to guide sustainable urban transformation design and course-correcting actions in a timely manner. Moreover, the uncertainties in the available methodologies remain large (Gately and Hutyra, 2017), with a recent study indicating under-reporting of the self-reported inventories of U.S. cities on average by 18.3 % (Gurney et al., 2021). Independent information coming from atmospheric observations is needed to evaluate urban inventories, but this also requires the advancement of the BU methodologies in terms of spatial and temporal resolution, as well as including all surface flux components contributing to the observations (Gurney et al., 2012, 2017; Lauvaux et al., 2020).

Recent studies have demonstrated the combined use of high spatio-temporal resolution BU emission models with tower-based measurements of CO₂ (and other trace gases) concentrations to derive optimised estimations of urban emissions within data assimilation schemes (e.g. Lauvaux et al., 2016, 2020; Lian et al., 2022; McKain et al., 2012; Stauffer et al., 2016). These approaches, commonly referred to as atmospheric inversions, use atmospheric transport modelling to assimilate the observed atmospheric concentrations and constrain the surface flux estimations derived by the BU models within Bayesian inversion systems (Tarantola, 2005). A concise overview of data assimilation systems for urban GHG monitoring is provided in a recent World Meteorological Organization (WMO) report for good practice guidelines (WMO, 2022). Bayesian inference is a powerful tool for probabilistic model calibration and inversion. It provides a comprehensive framework for combining information about the model parameters prior to observations with information obtained from experimental data. A Bayesian inversion framework provides the significant advantage that the solution to the inverse problem is a set of probability density functions (pdfs), rather than single numerical estimates of the inferred parameters. The pdf properties can therefore be used for the quantification of the uncertainty associated to each model parameter. The term “optimisation” is widely used in the data assimilation and atmospheric inversion literature to describe the result of the inversion process since the model priors are usually the BU model flux estimations and the inversion seeks to “optimise” these estimates according to the observations (e.g. Lauvaux et al., 2016, 2020; Lian et al., 2022; WMO, 2022). Within this framework, the Bayesian inversion is usually applied independently on short temporal cycles (e.g. 5-day, weekly or monthly) over segregated observation and prior datasets (e.g. hourly), as a result of a trade-off between capturing the effects of short time scale events (e.g. extreme cold, heatwaves, holidays, festivals) on the urban CO₂ fluxes and having enough data variability to solve the inversion problem. Most urban atmospheric inversion studies reach 1–2 km resolution within extended model domains to include the greater city boundaries and focus on annual whole-city emissions, lacking information on individual sectors

of the economy. Only few of them have attempted to discriminate between emissions from different sectors and take into account the contribution of biogenic flux components (Lauvaux et al., 2020; Wu et al., 2018). The atmospheric inversion methodologies are commonly limited by errors in atmospheric transport modelling (Díaz Isaac et al., 2014; Lauvaux et al., 2016), incorrect characterization of prior flux errors (Koohkan and Bocquet, 2012), and the number of atmospheric measurements available over the region of interest (Lauvaux et al., 2016, 2020).

Direct CO₂ flux observations by urban eddy covariance (EC) towers have been increasingly used to measure urban emissions and to investigate the underlying processes that contribute to diurnal and seasonal pattern of the total CO₂ balance (e.g. Björkegren and Grimmond, 2018; Davis et al., 2017; Lietzke et al., 2015; Nemitz et al., 2002; Nicolini et al., 2022; Schmutz et al., 2016; Stagakis et al., 2019). EC observations have been related to traffic emissions (Hiller et al., 2011; Järvi et al., 2012; Menzer and McFadden, 2017), heating degree days (Lietzke et al., 2015), and urban biogenic carbon fluxes (Bellucco et al., 2017; Velasco et al., 2016). However, most of the urban EC studies are restricted to a small part of the city, defined by the tower source area, which typically ranges 500–1000 m around the tower location (Feigenwinter et al., 2012). In contrast to the typical horizontal homogeneity assumption of the EC applications over plant ecosystems (Aubinet et al., 2012), urban ecosystems present a non-uniform distribution of surface CO₂ sources and sinks and this heterogeneity exceeds the scale of the source area, resulting in constantly varying source/sink compositions according to wind direction and atmospheric stability regimes (Crawford and Christen, 2015; Stagakis et al., 2019). This complexity restricts the representativeness of the urban EC flux observations and furthermore makes the interpretation and temporal aggregation of the data challenging. Hence, even though EC data over natural landscapes have been widely used in data assimilation studies to optimise and calibrate biogenic CO₂ flux models (e.g. Knorr and Kattge, 2005; Kountouris et al., 2018; Minet et al., 2015), there are only few attempts in the literature where urban EC observations were used within wide-scale CO₂ flux studies (Christen et al., 2011; Järvi et al., 2019; Wu et al., 2022).

Linking urban EC flux measurements with detailed characterization of the source areas at fine temporal resolution can provide the means for a comprehensive decomposition of the measured fluxes into individual component processes (Crawford and Christen, 2015; Hiller et al., 2011; Stagakis et al., 2019), but also link EC observations with high-resolution BU urban flux models (Christen et al., 2011). Complex EC flux source area (footprint) models based on large-eddy simulations (LES), Lagrangian stochastic particle dispersion (LPD) models and combinations of the two have been used to resolve the complex flow structures within the urban canopy, such as the street canyon effects (e.g. canyon vortices, channelling, etc.) (Auvinen et al., 2017; Hellsten et al., 2015). However, such modelling approaches are not yet computationally efficient to be used in time-series analyses. Analytical models, on the other hand, are fast alternatives with low computational demand and their level of sophistication has considerably evolved to provide realistic 2-D estimates over a wide range of landscapes and boundary layer stratifications (Kljun et al., 2015). Such models introduce similar assumptions to the EC theory, i.e. stationarity over integration period, horizontal homogeneity of the flow and negligible advection (Kljun et al., 2015; Leclerc and Foken, 2014; Schmid, 2002; Vesala et al., 2008), thus their applicability is restricted by the same data quality control procedures as the EC flux observations (Aubinet et al., 2012).

A recent study over a highly heterogeneous subarctic ecosystem EC flux site demonstrated the use of EC observations and analytical flux footprint modelling to infer the spatial variability of sensible heat and CH₄ fluxes (Levy et al., 2020). The method introduced by Levy et al. (2020) used Bayesian inversion to calibrate the parameters of a hierarchical model which describes the responses of the fluxes to different independent variables (e.g. temperature, wind speed, solar radiation) in different surface types and different spatial regions (multi-level). Such approach could be potentially transferred to urban areas where the spatial heterogeneity is profound, but the definition of the flux responses to independent variables would be challenging in urban areas. The processes that control urban CO₂ fluxes are so diverse in time and space that any attempt to model them based on independent variables (e.g. urban morphology, land cover, human activity, population density, meteorology) would provide just a simplified representation of the actual spatiotemporal variability of the fluxes (Stagakis et al., 2023). This is a well-known problem of the urban BU models and therefore the inversion approaches over urban areas do not focus on calibrating BU model parameters but rather “optimising” the gridded BU flux estimations in short time cycles (e.g. weekly) to capture the spatial and temporal variabilities of the fluxes (e.g. Lauvaux et al., 2016, 2020; Lian et al., 2022; McKain et al., 2012; Staufer et al., 2016).

This study introduces for the first time a data assimilation scheme where urban EC observations are used to optimise the estimates of a high-resolution urban BU CO₂ flux model. The approach uses very high spatial (20 m) and temporal (1 h) resolution data to account for the rapidly changing mixture of anthropogenic and biogenic CO₂ fluxes across the EC footprints, using two urban EC sites located 1.6 km apart in an urban city centre. The methodology formulates a Bayesian inversion problem, connecting the gridded BU model flux estimations with EC observations through the analytical source area model FFP (Flux Footprint Prediction, Kljun et al., 2015) and treating each surface CO₂ flux component individually. The Bayesian framework provides probabilistic solutions to our problem, allowing to quantify the uncertainties of each output. The inversion is applied in weekly cycles and separates building heating emissions, commercial/industrial emissions, traffic emissions, human respiration emissions and the biogenic flux (i.e. the net exchange of plant respiration, soil respiration and photosynthesis), providing timely policy-relevant outputs. The approach treats the source/sink heterogeneity within the EC footprints as an advantage rather than an obstacle, gaining more knowledge about the spatial and temporal patterns of individual processes contributing to the observed fluxes. In contrast to the urban atmospheric inversion applications (e.g. Lauvaux et al., 2016, 2020; Lian et al., 2022; Staufer et al., 2016), our approach considers a smaller spatial domain due to the restricted coverage of flux footprints compared to concentration footprints (Vesala et al., 2008), but increases the spatial resolution and source partitioning. Moreover, the present approach avoids some of the complexities of the atmospheric inversions, such as the dependency on detailed boundary air inflow characterization, by using direct flux measurements. Nevertheless, methodology issues are in common to both approaches, such as the representativeness of the observations, the configuration of the prior pdfs and the assumptions on the spatial dependencies of the error structures (Lauvaux et al., 2020; McKain et al., 2012; Wu et al., 2016).

In this study, a Bayesian inversion is applied at weekly time step over a 3-year period, combining gridded CO₂ flux estimates from a BU model (described in Part 1: Stagakis et al., 2023) with EC CO₂ flux measurements from two urban tower sites, to derive optimised gridded CO₂ flux estimates for each urban flux component and their respective uncertainties. The objectives of this study are i) to investigate the potential of urban EC flux observations for informing spatial disaggregated information of surface CO₂ fluxes, ii) to develop and evaluate a novel data assimilation methodology for optimised representation of urban CO₂ fluxes, and iii) to examine the potentials and limitations of the approach to support local scale urban climate change mitigation actions.

2. Methods

2.1. Study area and eddy covariance stations

The study area is the city centre of Basel, Switzerland, defined by a rectangle of 3040 m × 2980 m which includes two eddy covariance (EC) stations (Fig. 1). The first EC station (BKLI) is located on an 18 m tower, installed on the roof of a 20 m university building and has been operational since 2004. The system is mounted on a vertical extension at the top of the tower, reaching a total receptor height of 39 m above street level. The second EC system (BAES) is located on the top of a building over a busy central square, operated since 2009. The system is installed on a flagpole on top of a small construction over the building's rooftop at 41 m above street level. System specifications are described in Table S.1 and more details on system set-ups, relations to local surroundings, maintenance, calibration and raw data logging can be found in Schmutz et al. (2016), Lietzke et al. (2015) and Lietzke and Vogt (2013).

The local surroundings of both stations are characterised by diverse land use typologies. The eastern part of BKLI (azimuth angles between 350°–200°) in a radius of ~400 m is occupied by university buildings and the university hospital (Fig. 1). This area is characterised by midrise buildings, significant vegetation fraction and a main road that crosses the east side of the BKLI building. At 280 m north of BKLI, a new high-rise university building has been constructed since 2017 but was not in use during the study period (2018–2020). Fig. 1 describes the extreme CO₂ source/sink spatial heterogeneity of this area captured by the BU model (Stagakis et al., 2023). University and hospital buildings produce very high CO₂ emissions, the main road is also a significant CO₂ source, while the green areas across the campus behave as CO₂ sinks. Beyond the university campus and towards south-east (>400 m), is the city centre, which is densely built and has very small vegetation fraction. The city centre behaves as a strong CO₂ source, even though the vehicle traffic is restricted and there are no main roads crossing through this area. At the west side of BKLI (azimuth angles between 200°–350°), there is a typical residential area with midrise buildings, private gardens and restricted vehicle traffic, where the CO₂ emissions are lower than from the university campus and the city centre (Fig. 1).

BAES is located in a business district at the south-east of the city centre. To the north and west of BAES (azimuth angles between 230°–80°), there is a busy square dominated by vehicle traffic emissions (Fig. 1). This square is a node for four main roads, two of them being exceptionally wide with several lanes and a green alley separating the lane directions. Beyond the square and the main roads towards north and west is a densely built area with midrise buildings and small vegetation fraction. A big green area is located 300 m north-east of BAES, but this area is not frequently covered by the flux footprint (Fig. 1). The south-east part of the BAES site (80°–230°) is a residential area with mid-rise and low-rise buildings with significant area covered by gardens. There is a mix of building emissions and carbon sequestration evident across this area (Fig. 1). A main road is crossing across the south-east direction, acting as the main CO₂ source. Beyond this area and 450–500 m towards south-west, the main train station is located with several big buildings and busy main roads crossing around it, demonstrating very high annual emissions. However, this area is hardly inside the tower footprint (Fig. 1).

2.2. Eddy covariance data processing

Raw EC data of both systems are processed at 30-min time-steps for the study period (2018–2020) using the EddyPro® Software v7.0.6 (LI-COR Inc.). The main processing steps include axis rotation for tilt correction using the double rotation method (Kaimal and Finnigan, 1994), linear detrending to extract turbulent fluctuations (Gash and Culf, 1996), covariance maximization for time-lag compensation between the gas analyser and the sonic anemometer (Fan et al., 1990) and density fluctuation compensation according to Webb et al. (1980).

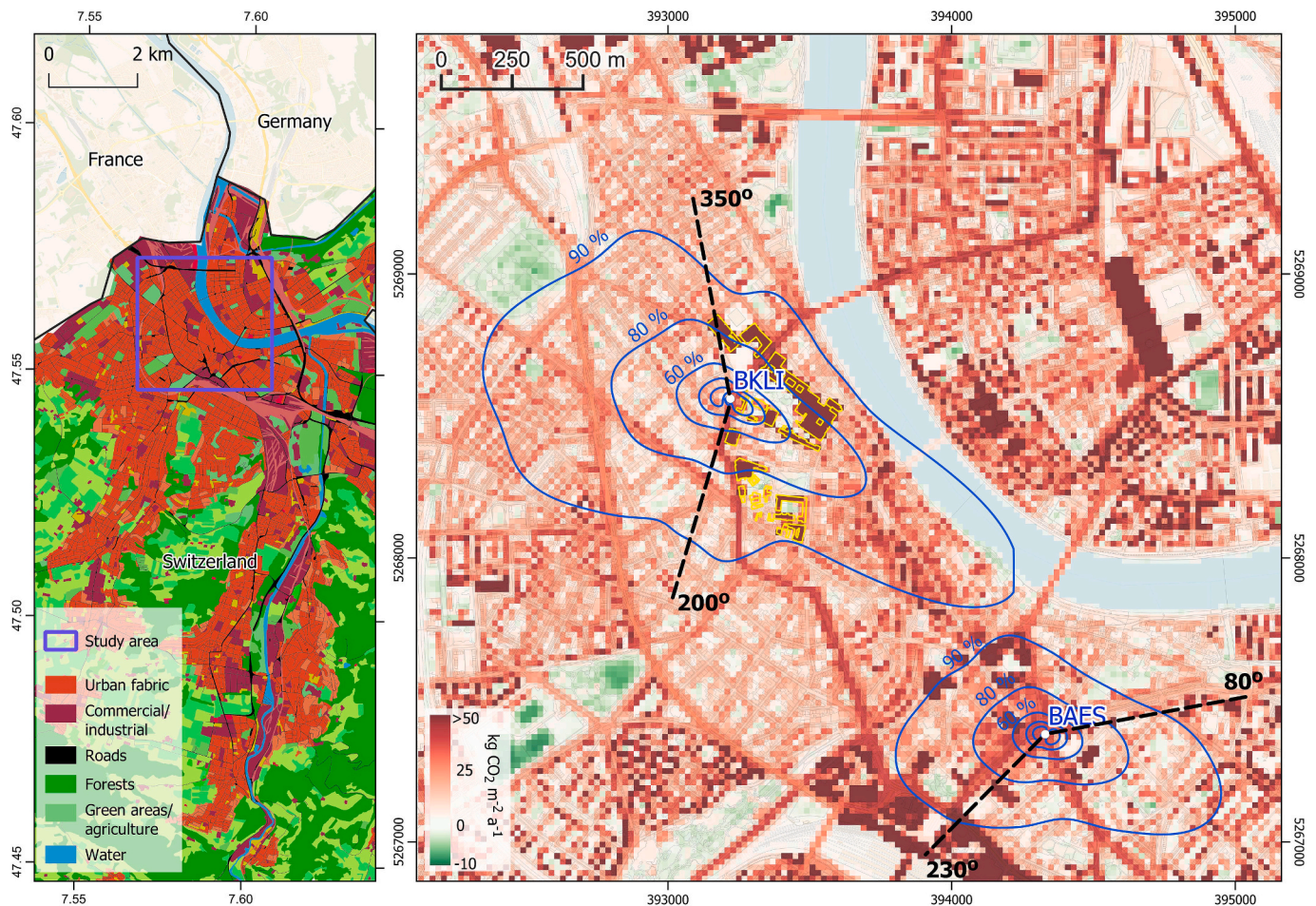


Fig. 1. The location of the study area (left) over an Urban Atlas land cover type representation. Urban Atlas land cover classes are merged for increasing the readability of the map. Eddy covariance site locations (right), along with the long-term source area isopleths, over the bottom-up modelled annual CO₂ flux map for 2018 (Stagakis et al., 2023) at 20 m resolution. The main wind direction sectors attributed to different land use profiles are indicated. University and hospital buildings are indicated with yellow polygons. All maps are projected at UTM 32N (EPSG: 32632).

Spectral corrections are also applied to flux estimates for low and high frequency losses. Analytic correction of high-pass filtering effects is applied according to Moncrieff et al. (2004) and correction of low-pass filtering effects is applied according to Moncrieff et al. (1997). Furthermore, statistical analyses are performed on the raw data to filter out spikes (Vickers and Mahrt, 1997), drop-outs and extreme values. Quality flagging is performed according to steady state and integral turbulence characteristics tests (Foken et al., 2004; Foken and Wichura, 1996; Göckede et al., 2008) based on the 3-point flagging system of Mauder and Foken (2004).

The produced net CO₂ flux ($F_{C,obs}$) time-series are filtered according to multiple criteria to avoid problematic values. Time-periods with the quality flag value of 2, around rain events (1 h before and 3 h after precipitation recordings) and during maintenance activities are rejected. Additionally, gas analyser warning flags are used as indicators of problematic measurements. If >10 % of the raw data are missing or flagged by any warning flag, then the values are rejected. For BKLI, the gas analyser is connected to the analogue input of the sonic, thus the gas analyser warning flags are not available. Instead, in BKLI, the standard deviation of CO₂ recordings during the flux interval is used as an indicator of problematic measurements. The thresholds are set to minimum: 0.001 mmol m⁻³, maximum: 0.5 mmol m⁻³. In BKLI, the wind sector $180^\circ \pm 15^\circ$ is also rejected to avoid wind distortion by the tower structure. In BAES, we did not reject any wind sector due to the thin structure of the supporting pole. F_C measurements under low turbulence situations are also removed from further analysis by setting a lower

threshold to friction velocity $u^* = 0.15 \text{ m s}^{-1}$ (e.g. Järvi et al., 2012; Matese et al., 2009; Salgueiro et al., 2020). The F_C data availability during the three-year period 2018–2020 after the filtering is similar for the two EC systems, reaching 64 %, where 3 % of data loss is due to maintenance and technical failures, 15.5 % is due to rain events and 17.5 % is due to the quality flags and the other filters.

2.3. Eddy covariance uncertainty

The Bayesian inversion framework requires a comprehensive specification of uncertainties. For the flux measurements, the random uncertainty (σ_{obs}) was estimated according to the method of Finkelstein and Sims (2001). This method deals with the sampling error of the EC measurements caused by the highly variable nature of turbulence and the limited number of independent samples during the sampling period. In contrast to systematic errors related to flow distortion or sensor separation, sampling error cannot be eliminated by careful system design or quality flagging and will always remain one of the largest sources of uncertainty (Businger, 1986; Finkelstein and Sims, 2001; Järvi et al., 2018). Sampling error is expressed as the variance of the EC measurements, which is the variance of the covariance. According to the method of Finkelstein and Sims (2001), auto- and cross-covariance between terms (i.e. vertical wind velocity and CO₂ concentration) are included in order not to underestimate the variance and produce relatively large error estimates compared to other approaches.

2.4. Source area modelling

The Flux Footprint Prediction model (Kljun et al., 2015) is used for the estimation of flux source areas for the two tower sites. FFP is an analytical footprint model that provides a 2-D representation of the flux source area according to surface morphological and atmospheric parameters. Digital Surface Models (DSMs) for buildings and trees, as well as a Digital Terrain Model (DTM) in 1 m resolution for the study area (Stagakis et al., 2023) are used as input for the Urban Multi-scale Environmental Predictor (UMEP) Morphometric Calculator tool (Lindberg et al., 2018) to estimate roughness length (z_0) and the zero-plane displacement height (z_d) around each EC site. The morphological inhomogeneity of the urban surroundings is considered in the source area modelling by adopting a directional roughness parameterisation scheme. z_0 and z_d are estimated anisotropically for all wind directions (averaged to 5° wind sectors) to a radius of 400 m around each EC tower according to the real urban surfaces parameterization of Kanda et al. (2013). Roughness parameter Look-Up-Tables (LUTs) are then developed for defining z_0 , z_d inputs to FFP according to wind direction. z_d is an indirect input for the model, since the measurement height is defined in FFP as $z_m = z_{\text{receptor}} - z_d$. As opposed to more conventional roughness parameterisation methods, such as Macdonald et al. (1998), Kanda et al. (2013) allows z_d to be higher than the mean building height (z_H), setting the upper limit to the maximum building height ($z_{H\text{max}}$), resulting to more spatially confined footprints than conventional methods. This way, the Kanda et al. (2013) roughness indicators seek to describe the effects of the pronounced building height variability to the roughness of the urban canopy and especially the disproportionate drag force generated by the tall buildings (Kent et al., 2017; Millward-Hopkins et al., 2011; Xie et al., 2008).

The other FFP inputs are i) wind direction, ii) standard deviation of lateral velocity fluctuations, iii) friction velocity (u^*), iv) Obukhov length (L) and v) planetary boundary layer height (PBLH). Wind attributes, u^* and L are calculated during the EC data processing. The Monin-Obukhov stability parameter (z_m/L) is used for the indication of atmospheric stability regime. PBLH is estimated for each 30 min period using diagnostic formulas to provide the initial height during night-time stable and neutral conditions (Nieuwstadt, 1981; Zilitinkevich et al., 2012) and then a simplified turbulence kinetic energy equation for convective conditions to determine the rate of change of PBLH for each 30-min period during convective daytime conditions (Batchvarova and Gryning, 1991).

FFP runs for each site at 1-hour time-step, considering two consecutive EC measurements as inputs on every run, at spatial domains of 2×2 km centred at each tower location and at 20 m spatial resolution. The gridded footprint function values $f_{l(x,y)}$ are normalized according to the domain sum to be used as spatial weighting grids ($\varphi_{l(x,y)}$):

$$\varphi_{l(x,y)} = \frac{f_{l(x,y)}}{\sum_{x,y=1}^N f_{l(x,y)}} \quad (1)$$

Where, l represents the tower site (BKLI or BAES), (x, y) represent the grid cells of the footprint and N represents the total number of grid cells at vertical and horizontal directions for the entire domain area of each footprint ($2 \text{ km} \times 2 \text{ km}$).

2.5. Bottom-up CO₂ flux modelling

Hourly building heating emission (E_B), commercial/industrial building emission (E_C), traffic emission (E_V), human respiration (R_H), soil respiration (R_S), plant respiration (R_V) and photosynthesis (P_V) estimates in 20 m resolution grid (x, y) are produced for the study area using the BU model described in Part 1 (Stagakis et al., 2023) for the study period (2018–2020). In this study we adopt the term anthropogenic emissions to describe the sum of E_B , E_C and E_V , while the biogenic

fluxes refer to the sum of the components R_S , R_V and P_V . R_H term is treated separately and it is not included in anthropogenic emissions or the biogenic fluxes. The BU model inputs are summarised in Fig. 2 and described in detail in Stagakis et al. (2023). In brief, the BU model is based on open geospatial datasets, census information, road traffic data and basic meteorological parameters. The main geospatial inputs are i) a detailed land cover map which discriminates building categories (i.e. residential, workplaces, mixed, commercial/industrial), road types (i.e. main roads, collecting roads, settlement roads, restricted traffic areas), paved surfaces and green areas, ii) high resolution Digital Surface Models (DSMs) for buildings and trees, iii) daytime and night-time population density maps, and iv) Leaf Area Index (LAI) time-series based on Copernicus Sentinel-2 (S2) imagery.

Continuous hourly traffic counts from multiple locations across the study area are used to estimate the traffic emissions (E_V) and simulate the population density dynamics, while in-situ measured meteorological parameters (air temperature, vapour pressure deficit, solar radiation, soil temperature, soil moisture) are used to drive the building space heating emission model (E_B) and the biogenic flux components (R_S , R_V , P_V). The building emission component E_C describes the extra emissions from commercial/industrial buildings due to their increased energy demand. Biogenic flux ($F_{C,B} = R_S + R_V - P_V$) is treated as one term in the inversion model (Section 2.6) due to the small effect of each biogenic process individually in the total EC-measured F_C and the difficulty to spatially and temporally discriminate the contributions of these processes.

2.6. Data assimilation

2.6.1. Inverse problem

EC-derived $F_{C,obs}$ are used to inform the BU model estimates (E_B , E_C , E_V , R_H , $F_{C,B}$) by employing a probabilistic inversion method (Bayesian inference) at a weekly cycle. The inversion model and its solution are implemented in MATLAB® (ver. R2019b, The MathWorks Inc., Natick, Massachusetts, USA) using the Bayesian Inference module of UQLab (Wagner et al., 2021). The inverse problem in our approach seeks to quantify the probability of the different scenarios where the $F_{C,obs}$ are explained by the BU model estimates. The comparison between the $F_{C,obs}$ and the hourly modelled gridded fluxes is achieved by spatially aggregating the gridded maps according to the normalized footprint functions (Eq. (1)). The forward model is formulated as:

$$F_{C,l} = \sum_{x,y=1}^N \varphi_{l(x,y)} \cdot [f_{B,l} \cdot E_{B(x,y)} \cdot S_B + f_{C,l} \cdot E_{C(x,y)} \cdot S_C + E_{V(x,y)} \cdot S_V + R_{H(x,y)} \cdot S_H + F_{C,B(x,y)} \cdot S_{Bio}] \quad (2)$$

Where, $F_{C,l}$ is a source area aggregated CO₂ flux model estimate; l represents the tower site (BKLI or BAES); (x, y) represent the grid cells of the footprint and flux products; N represents the total number of grid cells at vertical and horizontal resolution for the entire domain area of each footprint ($2 \text{ km} \times 2 \text{ km}$); $\varphi_{l(x,y)}$ is the footprint weighting grid of the same resolution as the BU model outputs (Eq. (1)); S_B , S_C , S_V , S_H , S_{Bio} are scaling factors for the respective gridded BU model outputs $E_{B(x,y)}$, $E_{C(x,y)}$, $E_{V(x,y)}$, $R_{H(x,y)}$, $F_{C,B(x,y)}$; and $f_{B,l}$, $f_{C,l}$ are normalization factors of the building emission maps as explained further below.

The UQLab feature of multiple forward models (Wagner et al., 2021) is used in this application (one model for each tower site, l). The two forward models depend on different subsets of input parameters. The input parameters which share the subscript l in Eq. (2) are different and independent for each forward model, while the ones that do not are treated as common for each inversion cycle.

The inversion solves for the set of the five scaling factors (S_B , S_C , S_V , S_H , S_{Bio}). These are introduced into the forward problem to simplify the inverse model formulation and solution. In our problem it is assumed that the different flux components (E_V , E_B , E_C , R_H , $F_{C,B}$) behave spatially

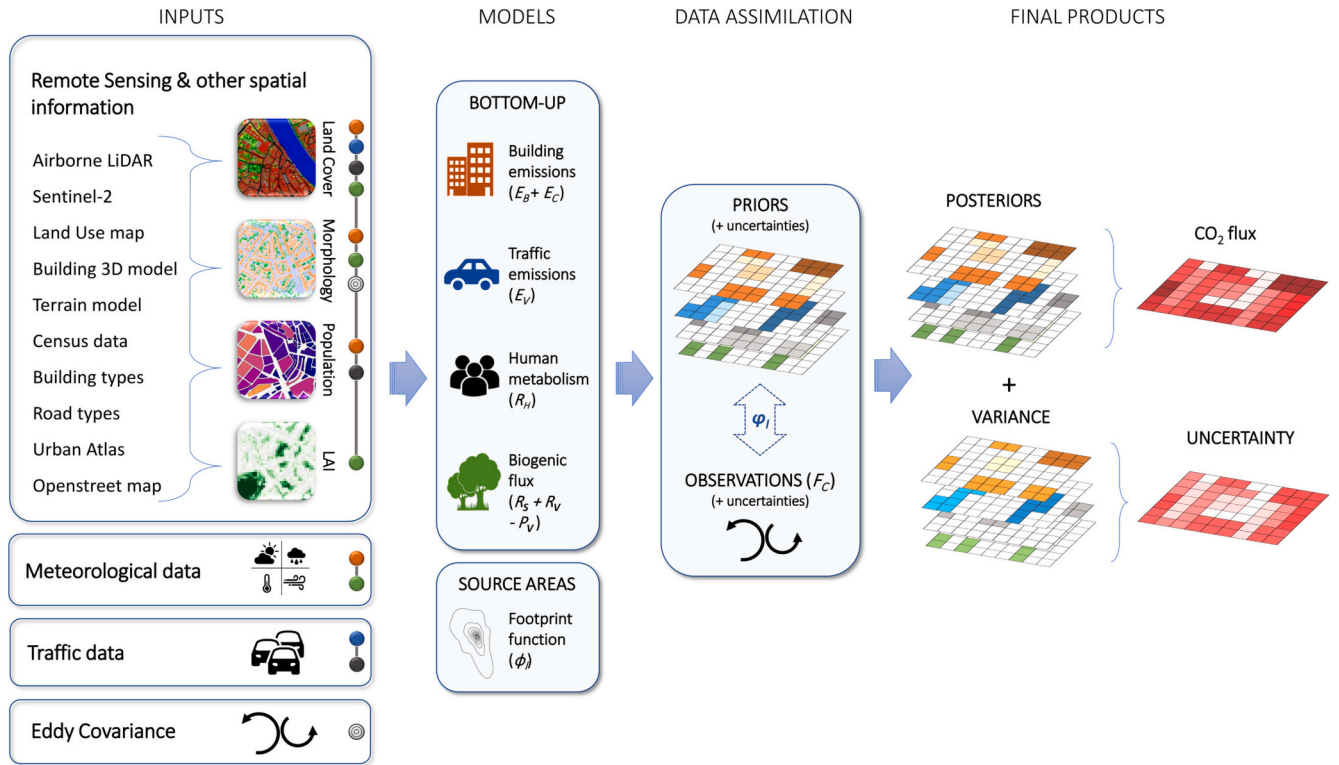


Fig. 2. Schematic representation of the methodology including the main data inputs, the models and the main outputs. The coloured circles next to each main input denote in which of the models each input is used (orange: building BU model, blue: traffic BU model, black: human respiration BU model, green: biogenic flux BU model, concentric cycles: flux footprint model). BU models and their inputs are described in detail in Part 1 (Stagakis et al., 2023).

homogeneously (i.e. uniform spatial error correlation) across the study area and therefore it is simpler to solve for five scaling factors instead for the gridded BU model outputs. The scaling factor prior distributions are defined as truncated Gaussian with μ (mean) = 1 and σ (standard deviation) = 0.6, constrained to the range [0–4]. S_H prior pdf is treated separately, with σ : 0.3 and boundaries [0–2], since R_H is not expected to present as high spatial and temporal variability as the rest of the flux components. The above prior pdf definition allows considerable flexibility in solving the inverse problem and accounts for the practical difficulty in quantifying the uncertainties of the BU models, as described in Stagakis et al. (2023). Previous urban studies have adopted similar approaches with a rather arbitrary definition of prior uncertainties (e.g. σ : 60 % of BU model outputs) (Lauvaux et al., 2016; Stauffer et al., 2016). Specifying rather large prior errors is a common approach to allow the inversion system to yield larger reductions of biases (Chevallier et al., 2012; Kountouris et al., 2015; Lauvaux et al., 2012).

The $f_{B,l}$ and $f_{C,l}$ normalization factors are used to account for the spatial variability of building emissions within the flux footprints. BU emissions models represent building emissions as spatially homogeneous across the building extents (Stagakis et al., 2023), whereas in reality the building emissions occur at specific points in space according to the location of the building or neighbourhood energy units and the respective chimneys. This inconsistency leads to overestimation of footprint-weighted E_B and E_C because building area is always present in flux footprints but actual building emissions are not necessarily within the footprint at all times. The following empirical formula is used:

$$f_{i,l} = \sum_{x,y=1}^{x,y=N} \lambda_{i(x,y)} \cdot M_{90(x,y)} / MAX_i \quad (3)$$

Where, $\lambda_{i(x,y)}$ represents the fraction of buildings according to the land cover map (i : B for non-commercial/industrial buildings, i : C for commercial/industrial buildings) at (x,y) grid cell; $M_{90(x,y)}$ is a spatial mask

of Boolean values (0,1) which defines the 90 % cumulative footprint area; and MAX_i is an empirical maximum value of accumulated building fractions which depends on the spatial resolution of the grid (x,y) . At 20-m resolution, MAX_B is set to 400 and MAX_C is set to 150. Eq. (3) follows the reasoning that when the atmospheric conditions favour spatially extended footprints towards building-occupied areas, then the probability of $F_{C,obs}$ to be affected by building emissions is higher than when the footprint is small and restricted near the tower location or directed towards open areas.

2.6.2. Observations and discrepancy model

The inversion system is designed to solve for weekly average flux components. However, for each weekly cycle, data are grouped in four different sets which are treated separately (i.e. separate inversions for each group). The groups are defined according to day type and hour, to i) weekday day (Monday–Friday, 08:00–17:00 CET), ii) weekday night (Monday–Friday, 18:00–07:00 CET), iii) weekend day (Saturday–Sunday, 08:00–17:00 CET) and iv) weekend night (Saturday–Sunday, 18:00–07:00 CET). Separate inversions are run for each weekly cycle for the weekday groups (i, ii) and for each 2-week cycle for the weekend data groups (iii, iv). The reason for running 2-week cycle inversions for the weekend data groups is because they do not contain enough hourly data per week. Even though two different time cycles are chosen, the posterior statistics from all inversions are combined to produce weekly fluxes as described in Section 2.7. The chosen weekly and 2-week cycles provide enough variability of each individual flux component captured by the observations due to the diurnal variability of each component (Stagakis et al., 2023) and furthermore due to the changing EC source areas according to wind direction. Additionally, the main wind fields (E – W) of the study area provide inverse source/sink typologies for each tower site (i.e. high emissions for BKLI and low emissions for BAES during E winds, and the opposite for W winds), therefore a variety of emission/sink composites are covered by the footprints of the two EC

sites even at persistent synoptic weather situations. At the same time, weekly inversion cycles are sufficiently short to capture the flux component variations on relatively short time scales due to events related to human behaviour (e.g. holidays, building heating patterns, commercial/industrial activities) or meteorological influences (e.g. heatwave or drought effects on biogenic fluxes). The separation of the weekly datasets to weekday/weekends and day/night is performed to investigate the effects of different human activity patterns on the CO₂ fluxes. It is expected that the emissions by buildings, traffic and even human respiration would present specific patterns according day type and hour of day, which are not simulated by the BU models but would potentially be captured by the observations.

A vector of observations $y_l = (y_{l,1}, \dots, y_{l,N_{out}})$ is defined for each forward model l and inversion dataset-cycle, $y_{l,i}$ being the hourly aggregated $F_{C,obs}$ of each tower l . The number of hourly observations over each inversion dataset-cycle (N_{out}) varies according to the missing EC data. Only the hourly periods when both tower observations are available are considered in the inversion to reduce the bias of the weekly posteriors towards site-specific characteristics. Inversions with <20 available EC observations (sum of both tower observations, $2 \cdot N_{out}$) are skipped, while the majority of the inversions run with 36 to 114 hourly observations (5 % - 95 % range), with an average of about 74.

The connection between the model predictions (Eq. (2)) and the hourly aggregated EC observations y_l is defined by the discrepancy (or error) model. A residual discrepancy vector $\varepsilon_l = (\varepsilon_{l,1}, \dots, \varepsilon_{l,N_{out}})$ of independent $\varepsilon_{l,i}$ is defined for each forward model l and inversion dataset-cycle according to the available observations (N_{out}). Each element of the residual vector $\varepsilon_{l,i}$ follows a Normal distribution with μ_i : 0 and σ_i^2 : the squared uncertainty of $F_{C,obs}$ (σ_{obs}^2 , hourly aggregated). The σ_{obs}^2 in our dataset varies between 0.5 and 95 (10 %–90 % range) with a median of 4.5 for both towers. A constant value of 5 is added to all σ_i^2 to account for the error inserted in the inversion problem by the forward model, which is essentially driven by uncertainties in the source area model and to a lesser extent by uncertainties in the normalization factors $f_{B,l}$ and $f_{C,l}$. Such a low and constant source area model error is chosen since σ_{obs}^2 estimations according to Finkelstein and Sims (2001) are already large enough to account for the source area model errors. Given that the discrepancy vector is based on the EC random error estimations, temporal error correlations are not considered in this application.

2.6.3. Sampling the posterior distributions

The computation of the posterior distributions is achieved using the Markov Chain Monte Carlo (MCMC) simulations technique (Robert and Casella, 2004; Liu, 2004). The adaptive Metropolis (AM) algorithm (Haario et al., 2001) is used, which starts as a standard random walk Metropolis algorithm (starting period, t_0), but the Gaussian proposal distribution of the classic Metropolis algorithm is tuned during the sampling procedure based on previously generated samples (Wagner et al., 2021). The proposal distribution of the standard random walk Metropolis algorithm is defined using a scaling factor of 0.1 to the prior marginal variances, as suggested by Wagner et al. (2021). To avoid singularity of the estimated covariance matrix, a small constant of 10^{-5} is added to the diagonal of its correlation matrix at each AM step. The AM runs in total with 3000 iterations and t_0 is set to 500 iterations. Following the common practice (Wagner et al., 2021), the first half of the sampling points are discarded (burn-in) before estimating the posterior distribution properties (i.e. μ_{post} , σ_{post}^2). The acceptance rate of the established model set-up is between 0.15 and 0.30 (5 %–95 % range), with a median of 0.25, which is near the optimal value to assume a well-tuned algorithm (Roberts et al., 1997).

2.7. Post-processing and evaluation

The weekly posterior gridded flux components and the respective

variances are calculated as:

$$E_{i,post(x,y)} = \frac{\sum_{L=1}^{L=4} H_L \cdot \mu_{i,L,post} \cdot E_{i,L(x,y)}}{168} \quad (4)$$

$$Var(E_{i,post})_{(x,y)} = \frac{\sum_{L=1}^{L=4} H_L \cdot \sigma_{i,L,post}^2 \cdot E_{i,L(x,y)}^2}{168} \quad (5)$$

Where, $E_{i,post}$ stands for the weekly posterior means of the 5 different flux components ($E_B, E_C, E_V, R_H, F_{C,B}$); L represents the different dataset - inversion per cycle (i.e. weekday day, weekday night, weekend day, weekend night); $\mu_{i,L,post}$ and $\sigma_{i,L,post}^2$ are the posterior mean and variance of the scaling factors ($S_B, S_C, S_V, S_H, S_{Bio}$) for each inversion L ; $E_{i,L}$ are the means of the 5 different BU-estimated flux components for each dataset L ; H_L is the number of hours per week for each inversion L (i.e. weekday day: 50, weekday night: 70, weekend day: 20, weekend night: 28); and 168 is the total number of hours per week. Since the weekend datasets run in 14-day cycles, Eq. (4) and Eq. (5) consider the same values of $\mu_{i,L,post}$, $\sigma_{i,L,post}^2$ and $E_{i,L}$ for two consecutive weekly cycles for L : weekend day and weekend night. Posterior data are not calculated for inversion cycles where at least one of the datasets L is absent due to limited observations. To avoid the bias of absent weekly data when aggregating to annual statistics, the time-series are first averaged per week and then per month for the three years. Weekly, monthly and yearly posterior variances are transformed to standard deviations (σ) per grid cell (x, y) to represent the respective uncertainties. We assume no temporal error correlations in our weekly outputs, therefore the temporally aggregated uncertainties are reduced by a factor of $1/\sqrt{N}$, N being the number of weeks used for each aggregation.

The inversion performance is assessed using the error reduction (ER) metric (e.g. Wu et al., 2018):

$$ER = (1 - \sigma_{post}/\sigma_{prior}) \cdot 100\% \quad (6)$$

Where, σ_{post} and σ_{prior} are the standard deviations of the posterior and prior distributions respectively. The ER metric represents the increase of confidence from prior to posterior state (Wu et al., 2018). Furthermore, source area aggregated $F_{C,post}$ and $F_{C,prior}$ are calculated for each inversion and tower site (BKLI, BAES) according to Eq. (2) using the posterior and prior mean values respectively, and compared against the $F_{C,obs}$ means for the respective periods. The statistical metrics used in this analysis are the root-mean-square error (RMSE), the mean absolute error (MAE), the bias and the linear regression slope, offset and coefficient of determination (R^2).

An extended analysis to investigate the inversion model results and overall behaviour is also performed by calculating $F_{C,post}$ and $F_{C,prior}$ at hourly time-step. In this analysis, the weekly posterior means of the scaling factors ($S_B, S_C, S_V, S_H, S_{Bio}$) are uniformly applied across each week on the hourly BU model priors. Hourly statistics are then derived for two different wind sectors and each EC site. Azimuth angles 350° and 200° define the wind sectors BKLI-E (east) and BKLI-W (west), while the angles 80° and 230° define the wind sectors BAES-E (east) and BAES-W (west) (Fig. 1). Data are also clustered according to seasons (roughly indicated as winter and summer) and type of day (weekdays, weekends). Summer period is considered as May to September and winter period includes the rest of the months.

3. Results

The results are structured in four sections. Weekly prior and posterior flux estimations are presented and compared in Sections 3.1 and 3.2 to examine the seasonal optimisation patterns of the data assimilation. The annually aggregated fluxes of priors and posteriors, as well as their uncertainties, are presented in Section 3.3. In the final section (Section 3.4), we present the model performance evaluation, where the model estimations (prior and posterior) are compared to F_C observations of the

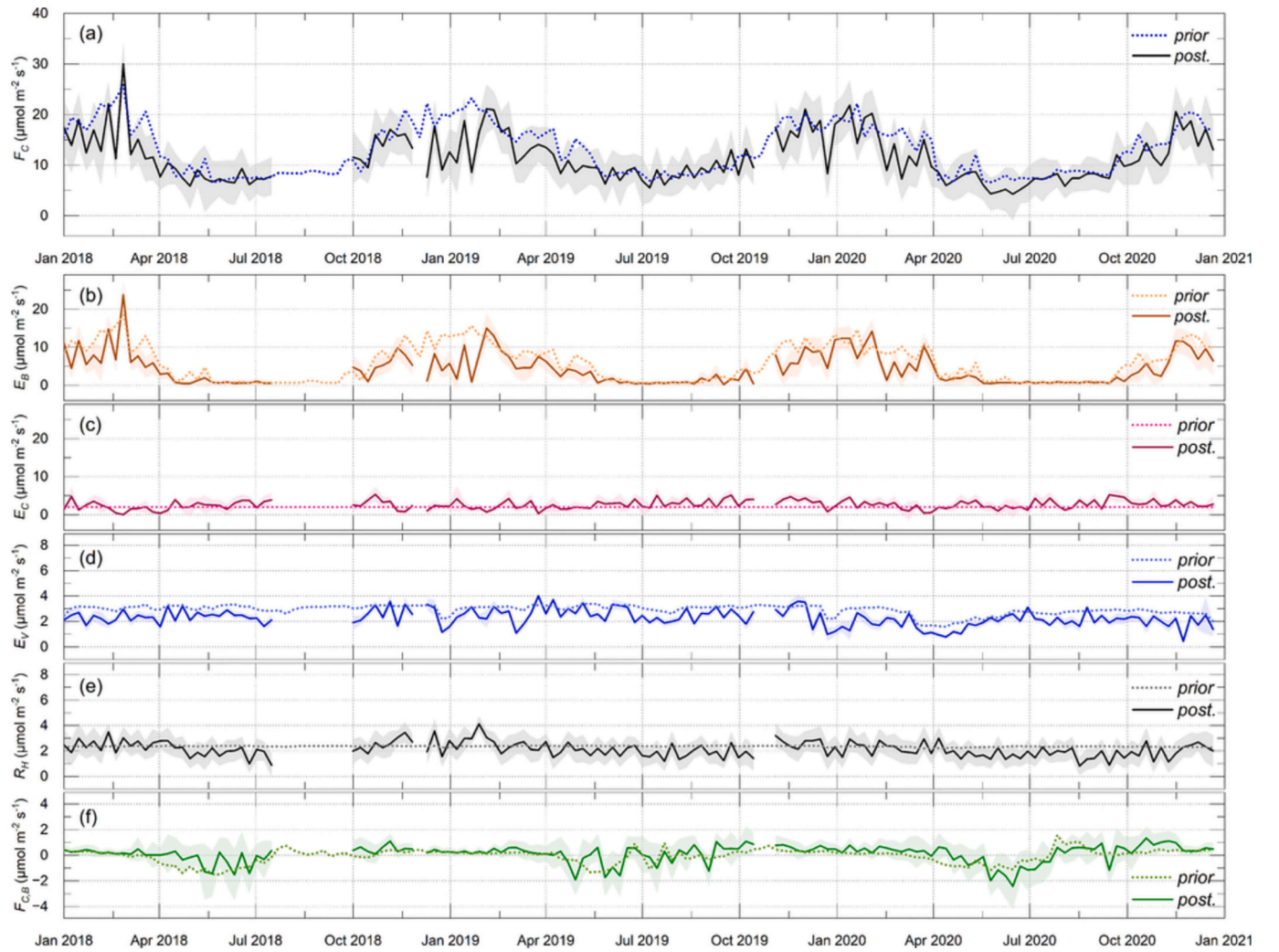


Fig. 3. Time-series of the prior and posterior weekly mean CO₂ flux for the study area ($\mu\text{mol CO}_2 \text{ m}^{-2} \text{ s}^{-1}$) and the period 2018–2020. (a) Total CO₂ flux (F_C), (b) building heating emissions (E_B), (c) commercial/industrial building emissions (E_C), (d) vehicle traffic emissions (E_V), (e) human respiration (R_H), and (f) biogenic flux ($F_{C,B}$) are presented separately. Note that y-axis scales are different between the different graphs. Shaded areas represent the posterior uncertainty (expressed as 2σ).

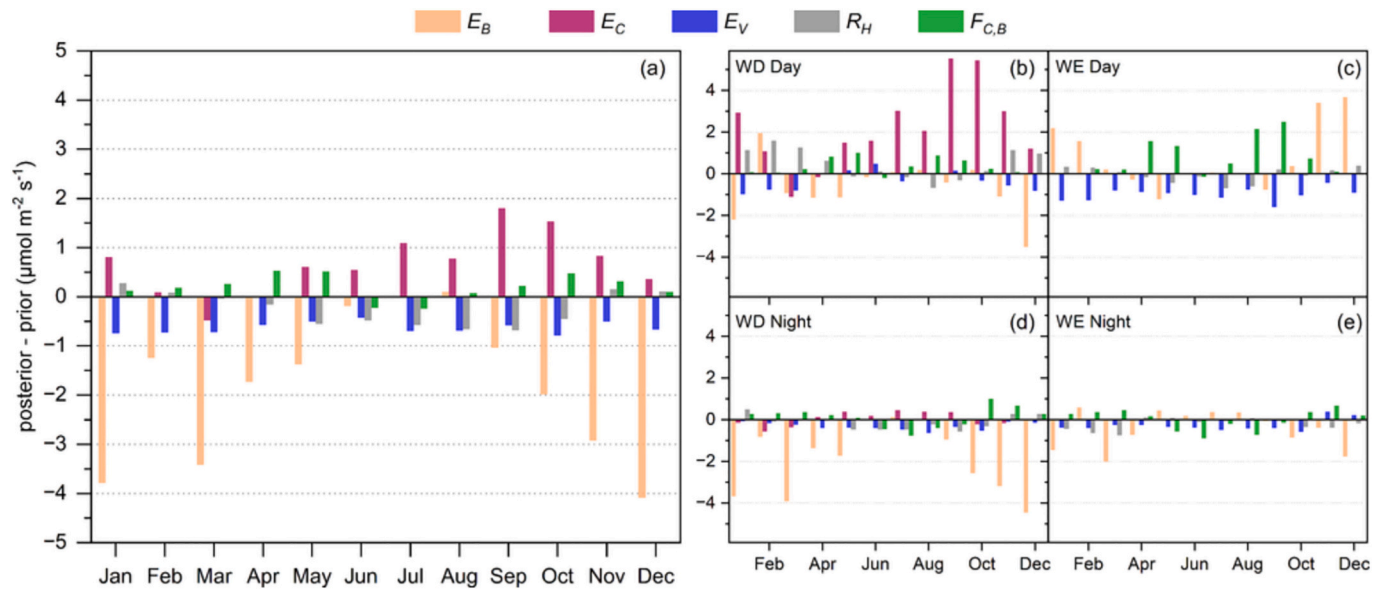


Fig. 4. Absolute differences between monthly mean prior and posterior CO₂ flux estimations ($\mu\text{mol CO}_2 \text{ m}^{-2} \text{ s}^{-1}$). The differences between (a) mean flux totals and the mean flux of the different inversion dataset: (b) weekday day, (c) weekend day, (d) weekday night, (d) weekend night, are presented separately.

Table 1

Annual flux totals ($\text{kg CO}_2 \text{ m}^{-2} \text{ year}^{-1}$) for the study area. Posterior uncertainties (σ) are included in the parentheses. The values represent the mean of the years 2018–2020.

		Priors	%	Posteriors	%
Building heating emissions	E_B	8.1	44.5	5.9 (± 0.04)	37.1 (± 0.3)
Commercial/Industrial emissions	E_C	2.8	15.4	3.7 (± 0.13)	23.3 (± 0.8)
Vehicle emissions	E_V	4.1	22.5	3.2 (± 0.04)	20.1 (± 0.3)
Human respiration	R_H	3.3	18.1	2.9 (± 0.08)	18.2 (± 0.5)
Biogenic flux	$F_{C,B}$	−0.1	−0.5	0.2 (± 0.10)	1.3 (± 0.6)
Total	F_C	18.2		15.9 (± 0.43)	

two EC towers. In this section, the analysis deals with source area aggregated fluxes, in contrast to the previous sections which present the flux estimates of the whole study area.

3.1. Modelled prior and posterior fluxes

Fig. 3 presents the time-series of weekly prior and posterior fluxes for the whole study area, as well as the posterior uncertainties represented as 2σ . There is intense seasonal variability in the total CO_2 flux (F_C) captured both by the prior and posterior estimations. The study area behaves as a CO_2 source during all seasons (Fig. 3a), while F_C is approximately doubled during winter following the pronounced rise of building emissions (E_B) due to space heating (Fig. 3b). There are significant changes in the weekly posterior E_B estimations compared to the prior during winter which drive E_B , and consequently F_C , towards lower emissions in most cases. This effect is especially pronounced during the winter of 2019 (Fig. 3b). Industrial/commercial emissions (E_C) do not present any seasonal cycle in the priors due to the BU model configuration, however, the posterior E_C estimations show some seasonal variability mainly towards higher emissions compared to the prior estimations (Fig. 3c). Traffic emissions (E_V) have low weekly variability in the prior, with some exceptions during Christmas holidays and the COVID19 lockdown period (March–May 2020) (Fig. 3d). Posterior E_V estimations are in general lower than the prior with more pronounced variability from week to week. Posterior E_V is driven even lower during Christmas holidays and the lockdown period. Similarly to E_C , prior human respiration (R_H) is constant during the whole year (Fig. 3e) due to the BU model configuration, however, the posterior estimations drive R_H to lower values during summer periods and in some cases to higher values during winter. Biogenic prior fluxes ($F_{C,B}$) have a clear seasonal pattern following meteorology and plant phenology (Stagakis et al., 2023) (Fig. 3e). Winter is a dormant period for all biogenic components and green areas behave as weak CO_2 sources. Photosynthesis rises during spring and peaks during early summer. During this period, green areas are behaving as carbon sinks. During late summer there is a decreasing tendency for plant productivity mainly due to drought conditions (Stagakis et al., 2023), which can be variable between different years. Posterior $F_{C,B}$ follows the same general patterns, with spring estimations sometimes higher and sometimes lower than the prior estimations. Late summer, autumn and winter posterior $F_{C,B}$ estimations are in general close to the priors with the tendency for higher values especially during winter.

The uncertainties of the F_C (Fig. 3a) and each flux component separately (Fig. 3b–f) provide insights into how well the inversion can constrain the different components. Even though the y-axis scaling of each graph is different, it is obvious that some flux components are determined with greater confidence than others during the inversion. R_H and $F_{C,B}$ show large uncertainties compared to the rest of the components, while E_B shows also high uncertainty during some periods. The best resolved flux component during the inversions is E_V , which shows low uncertainty during the whole study period. In all cases, the posterior errors are substantially lower than the prior errors. The error reduction statistics are summarised in Table S.2 and discussed further in Section 3.4.

3.2. Optimisation patterns

Seasonal optimisation patterns are investigated by calculating the mean monthly differences between prior and posterior estimations for each flux component and each inversion dataset (Fig. 4). The results reveal consistent seasonal patterns for each flux component which can largely be explained based on the BU model functionalities and the expected source/sink dynamics.

E_B is consistently reduced after the inversion throughout the year with stronger reductions occurring during the cold months (Fig. 4a), February being an exception. This seasonal pattern is particularly driven by the inversion results for weekday nights (Fig. 4d) and to a lesser extent by the results for weekend nights (Fig. 4e) and weekday days (Fig. 4b), indicating that the BU E_B model overestimates the emissions when temperature is low and especially during night-time. This is likely because the BU model does not account for diurnal and weekly building heating patterns, but instead follows the hourly air temperature variability (Stagakis et al., 2023) which tends to present daily minimums during night. Moreover, the BU model does not set any maximum threshold to E_B estimations during very low temperatures and therefore E_B priors could be excessively high during cold nights. Weekend night E_B reductions (Fig. 4e) are smaller than weekday night (Fig. 4d) and the weekend day pattern (Fig. 4c) is opposite to the general pattern (Fig. 4a), showing increased posterior E_B during cold months. These results most likely highlight the absence of the residential building heating schedules in the BU model, which are typically inverse to workhour patterns with higher residential emissions during weekends (Gurney et al., 2012).

E_C optimisation shows a consistent pattern towards higher emissions, especially during autumn and summer months (Fig. 4a). This pattern is driven by the weekday day results (Fig. 4b) due to the BU model configuration assuming zero E_C outside workhours (Stagakis et al., 2023), which prevents the ability of the inversion to adjust E_C outside workhours. The inversion results indicate that prior E_C is underestimated during nearly the whole year and especially during September and October. This seasonal pattern is possibly related to the local fuel consumption patterns by the commercial/industrial buildings that are within the EC source areas, which are mainly the hospital and university buildings around BKLI site (Fig. 1). These buildings use both district heating and local fuel consumption to fulfil their energy needs. Our results indicate that the balance between the two energy sources across the year is driving more local fuel consumption during summer and early autumn.

E_V optimisation is following a consistent pattern towards lower emissions throughout the whole year (Fig. 4a). This reduction is most obvious on weekend days (Fig. 4c). This indicates that E_V is overestimated by the BU model mainly during weekends, which may be explained by the deficiency of the BU model not considering driving conditions in the traffic emission factors (Stagakis et al., 2023). Assuming constant emission factors provides a linear relationship between traffic counts and CO_2 emissions which is not realistic due to the effects of congestion on driving mode (Ericsson, 2001). Hence, the E_V optimisation seems to account for the decreased emissions when traffic is close to free-flow conditions during weekends.

The general R_H optimisation pattern follows a decreasing trend

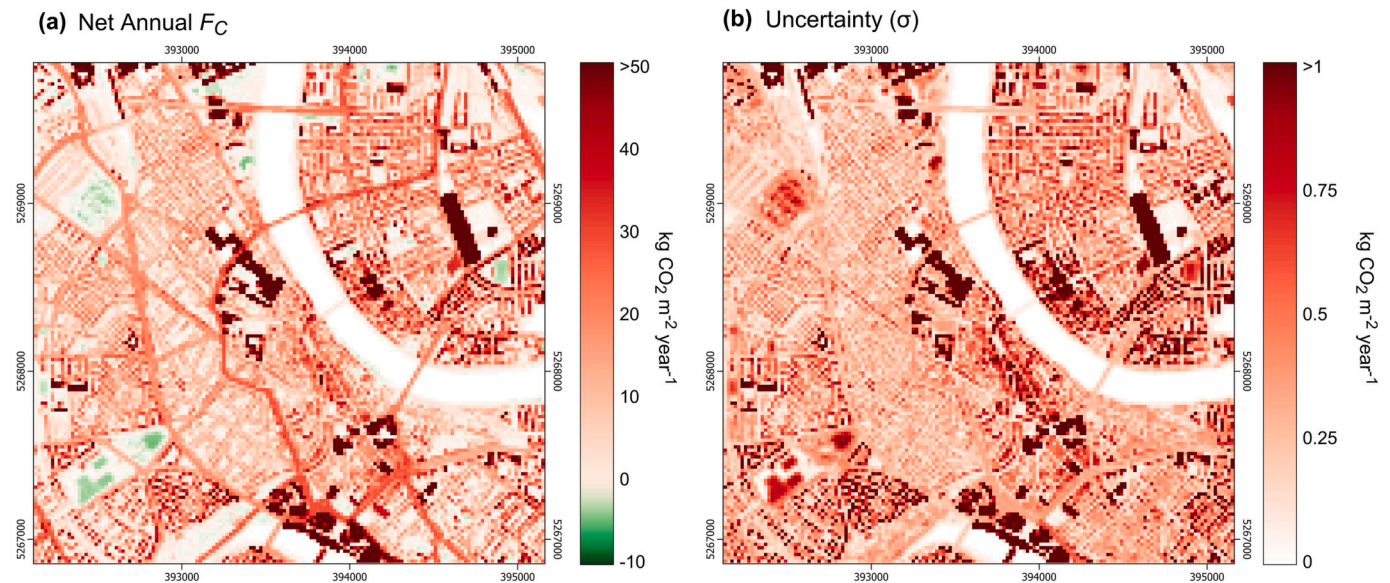


Fig. 5. Maps of temporally aggregated posterior (a) annual flux and (b) uncertainty (σ) in $\text{kg CO}_2 \text{ m}^{-2} \text{ s}^{-1}$. The maps represent the mean of the years 2018–2020.

during summer months and slightly increasing trend during winter (Fig. 4a). This pattern is driven mainly by the daytime results (Fig. 4b,c) and potentially reflects the combined effect of the seasonal changes in the incoming working population in the city centre during weekdays and the reduction of both local residents and employees during summer holidays. Such complex population density dynamics within the city centre were not accounted by the BU model (Stagakis et al., 2023).

$F_{C,B}$ optimisation patterns provide interesting insights into the BU modelled photosynthesis and respiration. The daytime optimisation patterns (Fig. 4b,c) indicate that during spring (April, May) and late summer (August, September) photosynthesis tends to be overestimated (i.e. towards lower flux values) by the BU model. The night-time optimisation patterns (Fig. 4d,e) show a symmetrical seasonal trend towards higher respiration during winter and lower during summer, pointing at a deficiency in the temperature control parameterisation of the BU respiration model. In total, $F_{C,B}$ is optimised towards higher values during winter, spring and autumn and towards lower values, i.e. more uptake, only during June and July (Fig. 4a).

Even though many of the optimisation patterns can be explained by known deficiencies in the BU model not fully reflecting the true source/sink dynamics, it is also possible that different emission types are sometimes confounded during the inversions since it is challenging to disentangle different emissions types when their signals co-vary because they originate from the same areas. An indication for this type of problems is the stronger increase of $F_{C,B}$ in April, May, August and September during weekend daytime (Fig. 4c) compared to weekday daytime (Fig. 4b). The excessive $F_{C,B}$ increase during weekend may be a compensation for the absence of E_C or other unaccounted CO_2 sources during weekends. Confounding signals in optimisation patterns are further discussed in Section 4.4. Other error sources to the optimisation results would include the effects of storage and advection fluxes on $F_{C,obs}$ and are discussed in Section 4.1.

3.3. Aggregated flux totals

Prior and posterior estimates of the annual flux totals are presented in Table 1. Anthropogenic emissions ($E_B + E_C + E_V$) have decreased by 14.7 % after the inversion. Even though E_C shows a significant increase (32.1 %), this increase is compensated by the rest of the anthropogenic sources which show decreases of 27.2 % and 22 % for E_B and E_V respectively. R_H has also decreased by 12.1 % and $F_{C,B}$ is transformed from a weak sink to a weak source across the study area. In total, F_C has

decreased by 12.6 %. The posterior estimations show that building emissions contribute 60.4 %, vehicle emissions 20.1 %, human respiration 18.2 % and biogenic components 1.3 % to the annual total flux of the study area (Table 1).

The temporally aggregated mean annual flux map of the posterior estimates and the respective uncertainty are presented in Fig. 5. Across the study area, emission hot-spots are concentrated in densely-built areas such as the city centre, at industrial/commercial buildings such as the university hospital and at very busy roads such as the area around the main train station (Fig. 5a). There are also several areas acting as sinks across the study area, which are mainly the parks, big gardens and some sport areas. The sequestration potential of areas with a mix of biogenic and anthropogenic components, such as street alleys and small gardens, is entirely counterbalanced by the anthropogenic emissions and human respiration. Moreover, as explicitly demonstrated also in Stagakis et al. (2023), there are several green areas scattered across the city where the ecosystem respiration components are already higher than the gross photosynthetic capacity, therefore acting as sources even without the anthropogenic component contribution.

The uncertainty map (Fig. 5b) shows that uncertainties in the annual scale are highest in industrial/commercial buildings and at residential buildings located in neighbourhoods with high local building emissions (i.e. low district heating coverage). Uncertainties over main roads are not so pronounced, while the uncertainties over the green areas that act as sinks are relatively high compared to roads and low-emission residential areas. The spatial patterns of uncertainty follow the magnitudes of the different flux components but also reflect the error reductions accomplished during the inversion (Table S.2). As discussed in more detail in Section 3.4, traffic emissions are determined with greater confidence than the other flux components during the inversion, while the biogenic fluxes show smaller error reductions than the anthropogenic emissions.

3.4. Model evaluation

The ER metric statistics for each flux component and inversion dataset are presented in Table S.2. Overall, ER values are adequately high for the majority of the inversions, indicating a well-behaving inversion model which is successfully constrained according to the observations. ER is moderate for E_B and E_C (medians between 57 %–73 %), somewhat lower for R_H and $F_{C,B}$ (medians between 29 %–57 %), but very high for E_V (medians between 87 %–92 %), revealing that traffic

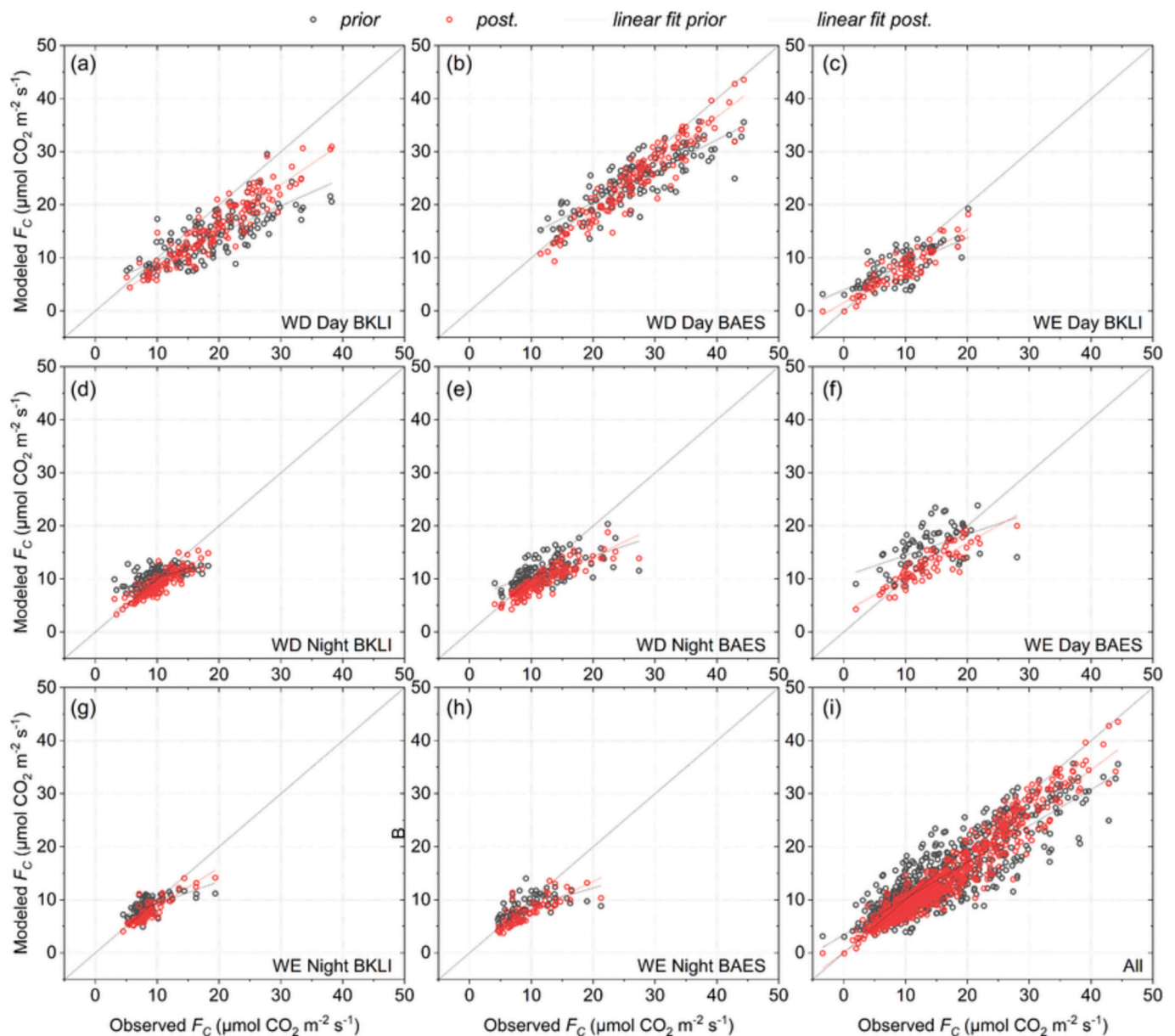


Fig. 6. Scatterplots between the eddy covariance measured F_C ($F_{C,obs}$) and the modelled source area aggregated F_C priors ($F_{C,prior}$) and posteriors ($F_{C,post}$) for the different inversion datasets of each eddy covariance site (BKLI, BAES) and altogether.

emissions are estimated with the highest confidence among the flux components. The ER of E_B and $F_{C,B}$ present distinctive seasonal patterns following each component's flux magnitudes, with low ER during summer and high during winter for E_B and the inverse seasonal pattern for $F_{C,B}$.

The inversion model behaviour is further examined by comparing the observations of the two tower sites ($F_{C,obs}$) with the source area aggregated modelled fluxes according to Eq. (2) for the prior and posterior estimates ($F_{C,prior}$, $F_{C,post}$) across the different inversion datasets. The scatterplots are presented in Fig. 6 and the evaluation metrics in Table S.3. The general tendency is that the posterior estimates show smaller error metrics compared to the prior and the linear regression lines of the posterior are closer to the 1:1 line. RMSE and MAE show considerable reduction after the inversions nearly for all datasets (Table S.3). RMSE ranges between 2.1 and 6.8 $\mu\text{mol CO}_2 \text{ m}^{-2} \text{ s}^{-1}$ for the prior and between 1.6 and 4.8 $\mu\text{mol CO}_2 \text{ m}^{-2} \text{ s}^{-1}$ for the posterior outputs. It is important to note that the magnitude of the posterior RMSE from this analysis is close to the weekly posterior uncertainties (σ) for F_C (1.0–3.3

$\mu\text{mol CO}_2 \text{ m}^{-2} \text{ s}^{-1}$), supporting the validity of our inversion results. The night-time inversions for the site BAES are the only ones that do not show considerable reduction of the error metrics after the inversions (Table S.3, Fig. 6e,h). Even though the error metrics improve after the inversions, the bias is not always smaller for the posterior estimates (Table S.3). Prior estimations tend to be overestimated during periods when flux magnitudes are medium or small, and underestimated when flux magnitudes are high, driving the slopes of the linear regressions towards low values (0.34–0.59) and the offsets towards high values (3.92–10.48). The inversions seem very efficient in solving the overestimation of the low – medium magnitude flux periods (especially during night-time and weekend inversions), however the underestimation of the high flux periods is still obvious in the posterior estimates. Hence, the linear regressions of the posteriors show higher slopes and smaller offsets than the priors, but still are not parallel to the 1:1. This also drives the bias to be always negative for the posteriors and sometimes even higher in magnitude than the priors. Higher absolute posterior biases are consistently apparent for the night-time inversions for

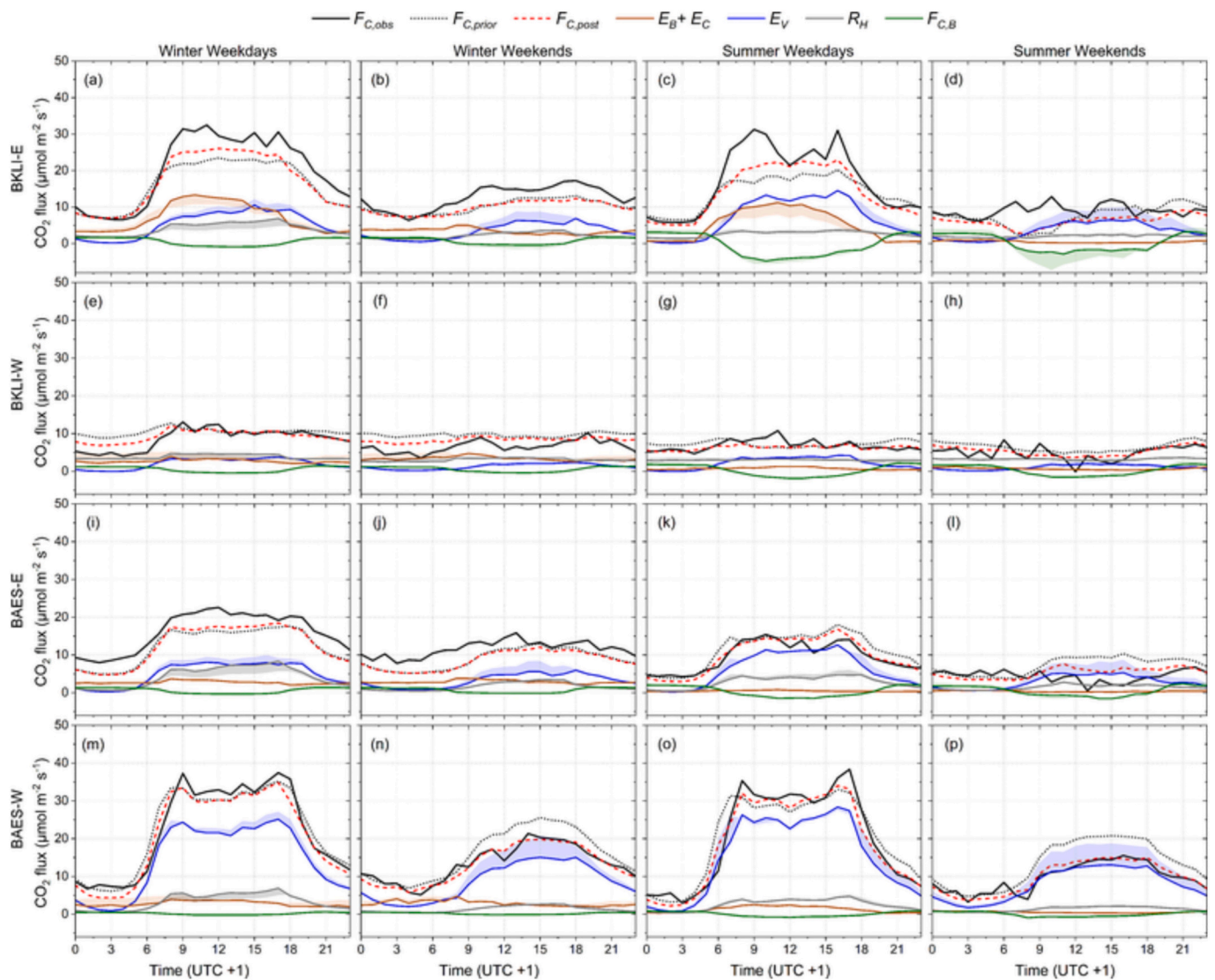


Fig. 7. Diurnal hourly mean profiles of eddy covariance measured F_C ($F_{C,obs}$) and source area aggregated modelled F_C for prior ($F_{C,prior}$) and posterior ($F_{C,post}$) estimations, as well as five modelled F_C components ($E_B + E_C$, E_V , R_H , $F_{C,B}$). For the latter, lines indicate the source area aggregated posterior estimations and the colour shading indicates the difference between prior and posterior profiles. The profiles are presented separately for winter weekdays (1st column), winter weekends (2nd column), summer weekdays (3rd column) and summer weekends (4th column) for the two wind sectors (W,E) of each eddy covariance site (BKLI, BAES).

both sites (Table S.3, Fig. 6d,e,g,h). Consequently, the inversion model solves efficiently only part of the prior deficiencies, leading to posteriors that still tend to be underestimated compared to the observations.

The hourly analysis of $F_{C,obs}$, $F_{C,prior}$ and $F_{C,post}$ provides further insights into the inversion results. Fig. 7 gives an overview of the mean diurnal profiles of the different wind sectors for the observed and modelled fluxes at different seasons and day types. Each wind sector has unique source/sink characteristics. BKLI-E is a mix of building and vehicle emissions, with E_C being an important emission component (Fig. 7a–d), BKLI-W is a residential sector without significant traffic or building emissions (Fig. 7e–h) and BAES (both wind sectors) is dominated by traffic emissions (Fig. 7i–p). There is a good agreement between $F_{C,post}$ and $F_{C,obs}$ in all wind sectors, with exceptional agreement demonstrated in the BAES-W (Fig. 7m–p), where E_V is the dominant emission source. The inversions have considerably improved the magnitudes and timing of diurnal $F_{C,post}$ in nearly all sectors and time-periods. However, inconsistencies between $F_{C,post}$ and $F_{C,obs}$ remain in some cases, such as BKLI-E (Fig. 7a–d) and BAES-E (Fig. 7i–l).

Even though posterior E_C has increased during weekday daytime, $F_{C,post}$ is not sufficiently increased to reach the $F_{C,obs}$ patterns of BKLI-E

(Fig. 7a,c). Moreover, BKLI-E $F_{C,post}$ during weekends is not adequately adjusted to match $F_{C,obs}$ patterns (Fig. 7b,d), especially during summer when an underestimation during morning hours is evident (Fig. 7d). As discussed also in Section 3.2, the weekend daytime inversions have reduced the vegetation photosynthesis disproportionately stronger compared to weekday inversions (obvious also in Fig. 7d), which is probably due to the summer weekend $F_{C,obs}$ pattern of BKLI-E. The latter cannot be explained during morning without taking into account some missing anthropogenic emissions, such as E_C .

The optimisation of E_V has been very efficient for matching $F_{C,post}$ with $F_{C,obs}$ in BAES-W (Fig. 7m–p). Night-time and weekend reductions of posterior E_V worked perfectly to match $F_{C,obs}$ patterns of this sector. On the other hand, the optimisation in the BAES-E sector did not improve the $F_{C,post}$ patterns so much, especially during winter (Fig. 7i,j). It is possible that E_B is underestimated in this wind sector, both by the prior and the posterior estimates. A common problem of the E_B BU model, which is difficult to solve by the inversion model in this study, is the spatial heterogeneity of the source/sink dynamics. Even though E_B reduction during winter night-time inversions work well for BKLI-W (Fig. 7e,f), this would not be necessarily beneficial for BAES-E (Fig. 7i)

because of the different heating systems across different neighbourhoods. The spatial heterogeneity and representativeness issues are discussed in more detail in Section 4.3.

4. Discussion

4.1. Eddy covariance observations

Previous studies that compared BU CO₂ flux estimations with EC-derived F_C observations in urban areas have exhibited differences of similar magnitude as the present study despite the different approaches used for the comparison. Christen et al. (2011) found absolute differences of monthly aggregated values between 0.6 and 4.1 $\mu\text{mol CO}_2 \text{ m}^{-2} \text{ s}^{-1}$ in a 2-year study in Vancouver, while Järvi et al. (2019) presented RMSEs between 0.5 and 5.6 $\mu\text{mol CO}_2 \text{ m}^{-2} \text{ s}^{-1}$ at four different sites/sectors across Helsinki for a 1-year evaluation period.

This study adopted a relatively strict quality control procedure to discard EC observations during non-ideal turbulent conditions (see Section 2.2). But still, EC measurements could be partly affected by the effects of CO₂ storage and horizontal advection, as well as the choices of the EC processing methods, such as coordinate rotation (Rannik et al., 2020). Storage within the urban volume below the measurement height is expected to be significant on hourly scales during night and early morning. Typically, diurnal storage flux variability would cause measured $F_{C,obs}$ to be underestimated during night and early morning with a subsequent overestimation during late morning hours when thermal mixing “flushes” stored CO₂ upwards towards the measurement height (Feigenwinter et al., 2012; Vogt et al., 2006). Storage fluxes have been quantified at a street canyon of Basel during a past study and found to vary between -3.4 (09:00) and $+2.5$ (21:00) $\mu\text{mol CO}_2 \text{ m}^{-2} \text{ s}^{-1}$ (Feigenwinter et al., 2012). In urban areas, CO₂ can also be stored within buildings, additionally to the outdoor air volume, which introduces an extra confounding factor in the storage flux which relates to the building ventilation patterns (Feigenwinter et al., 2012).

Storage fluxes could introduce bias to the inversion optimisation patterns of the present study. The night-time optimisation patterns towards lower E_B during the building heating period (Fig. 4d,e) could be partially due to storage fluxes. However, the night-time negative optimisation pattern is not so evident during weekends (Fig. 4e) compared to weekdays (Fig. 4d), which could either mean that storage fluxes are not so intense during weekends due to decreased anthropogenic emissions, or that storage is not a significant driver of the weekday optimisation patterns. Local scale advection fluxes could also affect EC measurements when the source areas are extremely patchy in terms of source/sink configuration (e.g. urban parks or water bodies mixed with built-up areas) and especially during stable atmospheric conditions when turbulent mixing is decreased. Given that the two EC sites in our study area are not located in patchy locations and furthermore by discarding all EC measurements which do not cover the turbulence criteria, we assume that the EC measurements used in the methodology are not significantly affected by local scale horizontal advection.

4.2. Source area modelling

Source area modelling in urban areas has been seldomly attempted in related literature (Christen et al., 2011; Crawford and Christen, 2015; Stagakis et al., 2019). This study adopts a detailed roughness parameterization of the urban surroundings according to Kanda et al. (2013) in order to simulate as realistically as possible the footprint extents using an analytical footprint model (Kljun et al., 2015). The present study has also tested the conventional Macdonald et al. (1998) roughness parameterisation, which resulted in lower hourly evaluation metrics (RMSE, MAE) between $F_{C,obs}$ and $F_{C,prior}$ (BKLI-E: 11.1, 7.8, BKLI-W: 8.5, 5.7, BAES-E: 8.7, 5.8, BAES-W: 11.7, 8.8), as opposed to the Kanda et al. (2013) roughness parameterisation (Stagakis et al., 2023), supporting the suitability of the latter in urban footprint modelling. Nonetheless, a

degree of uncertainty is expected to be introduced in the methodology through FFP estimations. Since FFP cannot resolve dispersion and flow structures within the urban canyon, it is expected that such effects could introduce bias in the inversion problem (Eq. (2)), especially regarding strong emissions that happen within urban canyons, such as E_V . A comparison between an LES-LDP generated footprint and an analytical model estimation in a simulation study over an urban-like canopy (Hellsten et al., 2015), finds that the analytical model is much more confined in the along-wind direction than the LES-LDP model when the measurement height is $1.8 \cdot z_H$ or higher. However, the analytical model cannot simulate the emissions from the street canyons in very close vicinity to the measurement location and the footprint peak contours are displaced tens of meters further along-wind than the LES-LDP. In a clear analogy, comparing LES-LDP and analytical footprint modelling over a real urban surface (Auvinen et al., 2017) revealed that the LES-LDP generated footprint exhibits a much more complex probability distribution and footprint peaks much closer to the tower location than the analytical model. In contrast to the simulation study of Hellsten et al. (2015), Auvinen et al. (2017) find that the LES-LDP footprint shows more pronounced spatial confinement in both directions (cross-wind and along-wind) than the analytical model. Both studies use a conventional roughness parameterisation of the analytical footprint model. The Kanda et al. (2013) parameterisation used in this study allows for much higher displacement heights (z_d) than the conventional methods, which lead to the more spatially confined footprints and peak functions much closer to the EC location. Hence, the analytical footprints would possibly be more comparable to the LES-LDP estimations of both studies (Auvinen et al., 2017; Hellsten et al., 2015) if the Kanda et al. (2013) parameterisation was used.

In addition to the challenges related to the complex flow structures within the urban canopy, footprint modelling in urban areas deals also with the spatial complexities of the building emissions. Depending on the neighbourhood energy use characteristics and building typologies, the locations and strengths of the point emissions from chimneys can be very variable. If the exact point locations are not known, as it is most probably the case in urban scale BU emission models, then spatial approximations of the building emissions are used (Stagakis et al., 2023) and therefore source area weighting introduces important uncertainty in the comparison between observations and models. Further uncertainty can also be introduced from the buoyant nature of plumes originating by strong building point sources, especially at elevated heights (i.e. above z_H) and during conditions of weak turbulence, which can cause either micro-scale effects to the EC measurements or divergence between the footprint-weighted emissions and the EC observations (Kotthaus and Grimmond, 2012). Avoiding such effects is important when selecting the location and height of the EC system (Feigenwinter et al., 2012). The EC locations of our study area do not have strong elevated point sources in close proximity. The empirical building emission normalization factors introduced in this paper (Eq. (3)) appear to be a sufficient solution to the aforementioned issues in our study area, yet unaccounted bias could be inserted in the model by this approach. Further investigation for determining more sophisticated and generalisable solutions to account for the variability of building emissions in space and time within urban flux footprint modelling are needed.

4.3. Spatial representativeness

The presented data assimilation methodology relies on two EC sites whose footprints cover part of the study area (Fig. 1), imposing challenges regarding their representativeness of the overall extent of the study area. When comparing the present approach to the atmospheric inversions, it is obvious that EC flux observations are more spatially restricted than the CO₂ concentrations (Vesala et al., 2008), but on the other hand, obtaining representativeness of the surface fluxes from concentration measurements is challenging and associated with multiple errors in the atmospheric modelling system (Lauvaux et al., 2016,

2020; McKain et al., 2012; Staufer et al., 2016). Increasing the sampling locations would appear beneficial for any observation-based approach, however, the locations, heights and number of the required instruments would depend on the methodological framework and the objectives of each study (Lauvaux et al., 2020; McKain et al., 2012; Wu et al., 2016). Lauvaux et al. (2016) investigated different atmospheric tower network configurations during the Indianapolis (INFLUX) experiment (Davis et al., 2017), concluding that the optimal design depends a lot on the underlying assumptions of prior spatial error correlations. If no spatial correlation is assumed, the inversion provides highly localised adjustments to the priors focused around each tower (i.e. within the observation footprints), which is highly unrealistic and spatially constrained (Lauvaux et al., 2016). Setting a “correct” correlation length is therefore very challenging and is inherently related to the emission types and the sophistication of the inversion set-up (Lauvaux et al., 2016; Wu et al., 2013).

An advantage of the selected site locations in the present study is that the directionality of the two sites across the main wind fields (E – W) is inverse, in the sense of high emission – low emission sectors, and therefore a variety of emission/sink composites are covered by the footprints of the two EC sites at each hour, increasing the representativeness of the observations during the weekly inversion periods. Since the present application considers a spatially restricted domain (Basel city centre) with similar urban typologies, it is assumed that the different flux components (E_V , E_B , E_C , R_H , $F_{C,B}$) behave spatially homogeneously (i.e. uniform spatial error correlation across the domain). Unlike the urban atmospheric inversions (Lauvaux et al., 2016, 2020; Lian et al., 2022; McKain et al., 2012; Staufer et al., 2016), our data assimilation method treats each flux component individually, advancing the level of precision in the results and the confidence regarding the spatial error covariances (Gurney et al., 2017; Lauvaux et al., 2016). Nevertheless, this assumption could introduce bias to the solution of the inverse problem, the spatial variability of the posteriors and lead to underestimated uncertainties per grid cell (Kaminski et al., 2001). To overcome such risks, our approach seeks to describe the spatial variability of the flux components in high resolution and as realistically as possible already from the BU modelling (Stagakis et al., 2023; Staufer et al., 2016). The most prominent example concerns E_V , which is a very important CO₂ source and highly variable spatially and temporally. The BU model considers the in-situ measured hourly traffic counts and assigns them to the respective road segments. Furthermore, the road types are classified to six different types according to traffic load to represent the different emission magnitudes (Stagakis et al., 2023). On the other hand, the spatial representation of E_C and E_B cannot be explicitly accurate within the BU model due to the significant emission variability across different types of building heating systems and industrial/commercial processes (Lauvaux et al., 2020; Stagakis et al., 2023), while the biogenic flux spatial variability is also challenging to describe and constrain in the complex and managed urban environment (Hardiman et al., 2017). Therefore, our assumption of uniform spatial error correlation across the domain for such components can lead to errors in the spatial representation of their posterior flux estimations.

4.4. Optimisation patterns

Correct source attribution during the inversion model is challenging when several different emission types originate from the same area. As briefly discussed in Section 3.2, $F_{C,B}$ disproportional increase during weekend daytime inversions in spring and late summer (Fig. 4c) is possibly a compensation for other emissions that are missing from the inversion set-up during weekends, such as E_C . Moreover, the increase of E_C during weekdays (Fig. 4b) is mainly driven by the observations in BKLI-E sector (Fig. 7a,c), where a strong mix of sources/sinks is evident. Part of the increasing E_C pattern may be caused due to the footprint model deficiency to account for the E_V emissions originating from the main road that crosses directly below the BKLI location. In contrast to

BAES, where E_V originates from a wide area around the EC location, E_V in the vicinity of BKLI is spatially confined mainly to a single urban canyon, which poses challenges to efficiently resolve with analytical footprint models as discussed in Section 4.2. On the other hand, the E_V -dominated BAES-W presents the more successful optimisation and F_C prediction (Fig. 7m–p), demonstrating that street-level emissions originating from wide open areas are efficiently captured by EC observations and analytical footprint models. The successful optimisation of BAES-W may also be in part due to the small fraction of building emissions and biogenic fluxes contributing to the EC signal (Fig. 7m–p), which could confound the inversion model as explained earlier.

In an analogy to our results, the study of Lauvaux et al. (2020) found that convergence in the traffic emissions was stronger than the building emissions and other stationary sources using a dense network atmospheric inversion methodology across the city of Indianapolis. Moreover, similar conclusions regarding the difficulty of the efficient discrimination of different emission types by inversion methodologies have been drawn by previous studies (Lauvaux et al., 2020; Nathan et al., 2018), suggesting the use of additional tracers (e.g. CO, ¹⁴C, stable C isotopes) to improve the attribution of sectoral biases.

5. Conclusions and future perspectives

This study presents for the first time a data assimilation approach of urban EC observations with very high resolution spatially disaggregated surface flux information derived by an advanced BU model. The developed methodology generates observation-evaluated and -calibrated estimates of each urban flux component individually and associated uncertainties at weekly time-step and 20 m resolution, providing valuable information for local scale climate policy design. The results of this study are very promising and reveal a great potential for further methodological advancements and upscaling.

It is demonstrated that EC is a highly valuable tool for understanding and monitoring local scale source and sink processes within the urban environment and can be efficiently used for evaluating and optimising high-resolution BU model estimates. EC observations are successfully combined and compared to the spatially disaggregated modelled information at weekly scale, with the RMSE ranging between 2.1 and 6.8 $\mu\text{mol CO}_2 \text{ m}^{-2} \text{ s}^{-1}$ for the prior model estimations and 1.6–4.8 $\mu\text{mol CO}_2 \text{ m}^{-2} \text{ s}^{-1}$ for the optimised model outputs. The optimisation provided meaningful seasonal patterns, improving several deficiencies of the BU model estimates and providing more realistic flux dynamics, such as the diurnal variability of building heating and the seasonal changes in the commercial/industrial emissions and the human respiration. In total, the posterior estimates indicate lower annual emissions by 12.6 % compared to the prior estimation, due to the significant decrease of the residential building heating emissions, the traffic emissions and the human respiration emissions. The only urban flux component that was significantly increased after the inversions is the commercial/industrial emissions. Posterior flux uncertainties are significantly decreased after the inversion for all the flux components, with particularly strong reductions being evident for the traffic emissions. The error reduction was smaller for human respiration and biogenic fluxes compared to the anthropogenic emissions, indicating greater confidence of the inversions towards the latter.

Overall, the inversion methodology has brought the prior model estimates much closer to the observations, but a tendency for CO₂ flux underestimation is still obvious in the posteriors. It is demonstrated that the inversion methodology is more efficient when the urban structure and CO₂ source/sink mixture is less complex, such as BAES-W which is dominated by traffic emissions originating from a wide area. When strong building emissions are mixed with traffic originating from narrow urban canyon structures and with significant biogenic fluxes, such as BKLI-E, then the accurate decomposition of the flux observations becomes challenging. In such cases, different source types can be confounded and the inversion method may lose its efficacy.

Several scientific challenges for future methodological advancements are identified through the present study. The spatial representativeness of EC observations is inherently restricted, posing challenges in defining an optimal design regarding the tower site number and locations, as well as the spatial error structure assumptions in the inverse modelling. The present study reveals that the most critical errors in spatial representativeness are related to the flux components that are most difficult to predict by the BU models, such as building emissions and the biogenic fluxes. Involving more EC towers across the city and at areas of different source/sink compositions can help to assess and evaluate the optimal strategy and experimental structures in order to reduce the spatial biases. Tall-tower EC applications may also provide increased potential in data assimilation approaches, since they would provide fluxes of wide spatial and sectoral representativeness. Moreover, improving the prior estimations of the biogenic fluxes and building emissions can reduce the spatial biases introduced in the inversion model.

A significant methodological and technological challenge for the further advancement of EC data assimilation applications is the flux footprint modelling in complex terrain and source/sink landscapes, such as urban areas. The analytical modelling approach adopted in the present methodology is a resource efficient alternative to the demanding LES and LPD models and is proved to be consistent when combining EC measurements with modelled high resolution flux maps. However, there are still limitations associated to the complexity of the urban structure and emission patterns that cannot be resolved by the analytical footprint model simulations. Developments in the field of LES-LPD modelling for urban areas are expected to improve future applications and provide better partitioning of the flux observations.

Finally, upscaling the presented methodology to simulate the total CO₂ emissions within the administrative level boundaries would require extending the model domain and account for several other land cover types and emission sources (e.g. industrial areas, agriculture, waste management, airports, etc.). There are technical restrictions in the present methodology to account for emissions that happen well beyond the urban canopy layer height, as well as to the areal extent which can be covered by EC observations. Combination of the presented approach with atmospheric inversion methodologies and tall-tower EC should be investigated in order to extend the model domain to city-wide emissions and build integrated observation-based monitoring systems that would resolve the underlying surface flux processes at different scales.

Funding

This research has received funding from the European Union's Horizon 2020 research and innovation programme under the Marie Skłodowska-Curie, grant agreement No 836443. Financial support from ICOS Switzerland (ICOS-CH) Phase 3 (Swiss National Science Foundation, grant 20F120_198227) is also acknowledged.

CRediT authorship contribution statement

Stavros Stagakis: Conceptualization, Formal analysis, Funding acquisition, Software, Investigation, Methodology, Validation, Visualization, Writing – original draft. **Christian Feigenwinter:** Data curation, Supervision, Writing – review & editing. **Roland Vogt:** Resources, Data curation, Supervision, Project administration, Writing – review & editing. **Dominik Brunner:** Methodology, Writing – review & editing. **Markus Kalberer:** Resources, Project administration, Writing – review & editing.

Declaration of competing interest

The authors declare that they have no known competing financial interests or personal relationships that could have appeared to influence the work reported in this paper.

Data availability

All datasets produced for the present study are available in Zenodo repository under Creative Commons Licence CC-BY-4.0:

- Land Cover (<https://doi.org/10.5281/zenodo.6511967>)
- Digital Surface Models (<https://doi.org/10.5281/zenodo.7189252>)
- Population density (<https://doi.org/10.5281/zenodo.7189315>)
- Leaf Area Index (<https://doi.org/10.5281/zenodo.7189509>)
- In-situ meteorological dataset (<https://doi.org/10.5281/zenodo.7189850>)
- Eddy covariance dataset (<https://doi.org/10.5281/zenodo.7573528>)
- CO₂ flux maps (<https://doi.org/10.5281/zenodo.7875386>)

Acknowledgements

Dr. Robert Spirig and Günter Bing (University of Basel) are acknowledged for their support in coding, database handling and other technical issues. Prof. Natascha Kljun (Lund University) is acknowledged for offering the FFP code freely accessible online (<https://footprint.kljun.net/>). Prof. Bruno Sudret and Dr. Stefano Marelli (ETH Zurich) are acknowledged for offering the UQLab modules completely open source (<https://www.uqlab.com/>). Two anonymous Reviewers are acknowledged for their valuable comments that helped to improve the manuscript.

Appendix A. Supplementary data

Supplementary data to this article can be found online at <https://doi.org/10.1016/j.scitotenv.2023.166035>.

References

- Aubinet, M., Vesala, T., Papale, D., 2012. *Eddy Covariance: A Practical Guide to Measurement and Data Analysis*, first ed. Springer, Dordrecht Heidelberg London New York.
- Auvinen, M., Järvi, L., Hellsten, A., Rannik, Ü., Vesala, T., 2017. Numerical framework for the computation of urban flux footprints employing large-eddy simulation and Lagrangian stochastic modeling. *Geosci. Model Dev.* 10, 4187–4205. <https://doi.org/10.5194/gmd-10-4187-2017>.
- Batchvarova, E., Gryning, S.E., 1991. Applied model for the growth of the daytime mixed layer. *Bound.-Layer Meteorol.* 56, 261–274. <https://doi.org/10.1007/BF00120423>.
- Bellucco, V., Marras, S., Grimmond, C.S.B., Järvi, L., Sirca, C., Spano, D., 2017. Modelling the biogenic CO₂ exchange in urban and non-urban ecosystems through the assessment of light-response curve parameters. *Agric. For. Meteorol.* 236, 113–122. <https://doi.org/10.1016/j.agrformet.2016.12.011>.
- Björkegren, A., Grimmond, C.S.B., 2018. Net carbon dioxide emissions from central London. *Urban Clim.* 23, 131–158. <https://doi.org/10.1016/j.uclim.2016.10.002>.
- Businger, J.A., 1986. Evaluation of the accuracy with which dry deposition can be measured with current micrometeorological techniques. *J. Clim. Appl. Meteorol.* 25, 1100–1124. [https://doi.org/10.1175/1520-0450\(1986\)025<1100:EOTAWW>2.0.CO;2](https://doi.org/10.1175/1520-0450(1986)025<1100:EOTAWW>2.0.CO;2).
- Chevallier, F., Wang, T., Ciais, P., Maignan, F., Bocquet, M., Altaf Arain, M., Cescatti, A., Chen, J., Dolman, A.J., Law, B.E., Margolis, H.A., Montagnani, L., Moors, E.J., 2012. What eddy-covariance measurements tell us about prior land flux errors in CO₂-flux inversion schemes. *Glob. Biogeochem. Cycles* 26. <https://doi.org/10.1029/2010GB003974>.
- Christen, A., Coops, N.C., Crawford, B.R., Kellett, R., Liss, K.N., Olchovski, I., Tooke, T.R., Van Der Laan, M., Voigt, J.A., 2011. Validation of modeled carbon-dioxide emissions from an urban neighborhood with direct eddy-covariance measurements. *Atmos. Environ.* 45, 6057–6069. <https://doi.org/10.1016/j.atmosenv.2011.07.040>.
- Crawford, B., Christen, A., 2015. Spatial source attribution of measured urban eddy covariance CO₂ fluxes. *Theor. Appl. Climatol.* 119, 733–755. <https://doi.org/10.1007/s00704-014-1124-0>.
- Davis, K.J., Deng, A., Lauvaux, T., Miles, N.L., Richardson, S.J., Sarmiento, D.P., Gurney, K.R., Hardesty, R.M., Bonin, T.A., Brewer, W.A., Lamb, B.K., Shepson, P.B., Harvey, R.M., Cambaliza, M.O., Sweeney, C., Turnbull, J.C., Whetstone, J., Karion, A., 2017. The Indianapolis flux experiment (INFLUX): a test-bed for developing urban greenhouse gas emission measurements. *Elementa* 5. <https://doi.org/10.1525/elementa.188>.
- Díaz Isaac, L.I., Lauvaux, T., Davis, K.J., Miles, N.L., Richardson, S.J., Jacobson, A.R., Andrews, A.E., 2014. Model-data comparison of MCI field campaign atmospheric

- CO₂ mole fractions. *J. Geophys. Res.* 119, 10536–10551. <https://doi.org/10.1002/2014JD021593>.
- Ericsson, E., 2001. Independent driving pattern factors and their influence on fuel-use and exhaust emission factors. *Transp. Res. Part D: Transp. Environ.* 6, 325–345. [https://doi.org/10.1016/S1361-9209\(01\)00003-7](https://doi.org/10.1016/S1361-9209(01)00003-7).
- Fan, S.-M., Wofsy, S.C., Bakwin, P.S., Jacob, D.J., Fitzjarrald, D.R., 1990. Atmosphere-biosphere exchange of CO₂ and O₃ in the central Amazon forest. *J. Geophys. Res.* 95 <https://doi.org/10.1029/jd095id10p16851>.
- Feigenwinter, C., Vogt, R., Christen, A., 2012. Eddy covariance measurements over urban areas. In: Aubinet, M., Vesala, T., Papale, D. (Eds.), *Eddy Covariance*. Springer Netherlands, Dordrecht, pp. 377–397. https://doi.org/10.1007/978-94-007-2351-1_16.
- Finkelstein, P.L., Sims, P.F., 2001. Sampling error in eddy correlation flux measurements. *J. Geophys. Res. Atmos.* 106, 3503–3509. <https://doi.org/10.1029/2000JD900731>.
- Foken, T., Wichura, B., 1996. Tools for quality assessment of surface-based flux measurements. *Agric. For. Meteorol.* 78, 83–105. [https://doi.org/10.1016/0168-1923\(95\)02248-1](https://doi.org/10.1016/0168-1923(95)02248-1).
- Foken, T., Göckede, M., Mauder, M., Mahrt, L., Amiro, B.D., Munger, J.W., 2004. Postfield data quality control. In: Lee, X., Massman, W.J., Law, B.E. (Eds.), *Handbook of Micrometeorology: A Guide for Surface Flux Measurements*. Kluwer Academic, Dordrecht, pp. 181–208. https://doi.org/10.1007/1-4020-2265-4_9.
- Gash, J.H.C., Culf, A.D., 1996. Applying a linear detrend to eddy correlation data in realtime. *Bound.-Layer Meteorol.* 79, 301–306. <https://doi.org/10.1007/BF00119443>.
- Gately, C.K., Hutrya, L.R., 2017. Large uncertainties in urban-scale carbon emissions. *J. Geophys. Res. Atmos.* 122, 11,242–11,260. <https://doi.org/10.1002/2017JD027359>.
- GCoM CRF, 2018. Global covenant of mayors: common reporting framework, Version 6.1, September 2018. https://www.globalcovenantofmayors.org/wp-content/uploads/2019/04/FINAL_Data-TWG_Reporting-Framework_website_FINAL-13-Sept-2018-for-translation.pdf.
- GHG Protocol, 2021. Global protocol for community-scale greenhouse gas inventories: an accounting and reporting standard for cities, version 1.1. https://ghgprotocol.org/sites/default/files/standards/GPC_Full_MASTER_RW_v7.pdf (accessed 24 June 2022).
- Göckede, M., Foken, T., Aubinet, M., Aurela, M., Banza, J., Bernhofer, C., Bonnefond, J. M., Brunet, Y., Carrara, A., Clement, R., Dellwik, E., Elbers, J., Eugster, W., Fuhrer, J., Granier, A., Grünwald, T., Heinesch, B., Janssens, I.A., Knohl, A., Koeble, R., Laurila, T., Longdoz, B., Manca, G., Marek, M., Markkanen, T., Mateus, J., Matteucci, G., Mauder, M., Migliavacca, M., Minerbi, S., Moncrieff, J., Montagnani, L., Moors, E., Ourcival, J.M., Papale, D., Pereira, J., Pilegaard, K., Pita, G., Rambal, S., Rebmann, C., Rodrigues, A., Rotenberg, E., Sanz, M.J., Sedlak, P., Seufert, G., Siebicke, L., Soussana, J.F., Valentini, R., Vesala, T., Verbeek, H., Yakir, D., 2008. Quality control of CarboEurope flux data - part 1: coupling footprint analyses with flux data quality assessment to evaluate sites in forest ecosystems. *Biogeosciences* 5, 433–450. <https://doi.org/10.5194/bg-5-433-2008>.
- Gurney, K.R., Razlivanov, I., Song, Y., Zhou, Y., Benes, B., Abdul-Massih, M., 2012. Quantification of fossil fuel CO₂ emissions on the building/street scale for a large U. S. City. *Environ. Sci. Technol.* 46, 12194–12202. <https://doi.org/10.1021/es3011282>.
- Gurney, K.R., Liang, J., Patarasuk, R., O'Keefe, D., Huang, J., Hutchins, M., Lauvaux, T., Turnbull, J.C., Shepson, P.B., 2017. Reconciling the differences between a bottom-up and inverse-estimated FFCO₂ emissions estimate in a large US urban area. *Elementa* 5. <https://doi.org/10.1525/elementa.137>.
- Gurney, K.R., Liang, J., Roest, G., Song, Y., Mueller, K., Lauvaux, T., 2021. Under-reporting of greenhouse gas emissions in U.S. cities. *Nat. Commun.* 12. <https://doi.org/10.1038/s41467-020-20871-0>.
- Haario, H., Saksman, E., Tamminen, J., 2001. An adaptive Metropolis algorithm. *Bernoulli* 7. <https://doi.org/10.2307/3318737>.
- Hardiman, B.S., Wang, J.A., Hutrya, L.R., Gately, C.K., Getson, J.M., Friedl, M.A., 2017. Accounting for urban biogenic fluxes in regional carbon budgets. *Sci. Total Environ.* 592, 366–372. <https://doi.org/10.1016/j.scitotenv.2017.03.028>.
- Hellsten, A., Luukkainen, S.M., Steinfeld, G., Kanani-Sühring, F., Markkanen, T., Järvi, L., Lento, J., Vesala, T., Raasch, S., 2015. Footprint evaluation for flux and concentration measurements for an urban-like canopy with coupled Lagrangian stochastic and large-Eddy simulation models. *Bound.-Layer Meteorol.* 157, 191–217. <https://doi.org/10.1007/s10546-015-0062-4>.
- Hiller, R.V., McFadden, J.P., Kljun, N., 2011. Interpreting CO₂ fluxes over a suburban Lawn: the influence of traffic emissions. *Bound.-Layer Meteorol.* 138, 215–230. <https://doi.org/10.1007/s10546-010-9558-0>.
- Hsu, A., Höhne, N., Kuramochi, T., Roelfsema, M., Weinfurter, A., Xie, Y., Lütkehermöller, K., Chan, S., Corfee-Morlot, J., Drost, P., Faria, P., Gardiner, A., Gordon, D.J., Hale, T., Hultman, N.E., Moorhead, J., Reuvers, S., Setzer, J., Singh, N., Weber, C., Widerberg, O., 2019. A research roadmap for quantifying non-state and subnational climate mitigation action. *Nat. Clim. Chang.* 9, 11–17. <https://doi.org/10.1038/s41558-018-0338-z>.
- IPCC, 2022. Climate change 2022: mitigation of climate change. Summary for policymakers. Contribution of working group III to the 6th assessment report of the intergovernmental panel on climate change. https://report.ipcc.ch/ar6wg3/pdf/IPCC_AR6_WGIII_SummaryForPolicymakers.pdf.
- Järvi, L., Nordbo, A., Junninen, H., Riikonen, A., Moilanen, J., Nikinmaa, E., Vesala, T., 2012. Seasonal and annual variation of carbon dioxide surface fluxes in Helsinki, Finland, in 2006–2010. *Atmos. Chem. Phys.* 12, 8475–8489. <https://doi.org/10.5194/acp-12-8475-2012>.
- Järvi, L., Rannik, U., Kokkonen, T.V., Kurppa, M., Karppinen, A., Kouznetsov, R.D., Rantala, P., Vesala, T., Wood, C.R., 2018. Uncertainty of eddy covariance flux measurements over an urban area based on two towers. *Atmos. Meas. Tech.* 11, 5421–5438. <https://doi.org/10.5194/amt-11-5421-2018>.
- Järvi, L., Havu, M., Ward, H.C., Bellucco, V., McFadden, J.P., Toivonen, T., Heikinheimo, V., Kolari, P., Riikonen, A., Grimmond, C.S.B., 2019. Spatial modeling of local-scale biogenic and anthropogenic carbon dioxide emissions in Helsinki. *J. Geophys. Res. Atmos.* 124, 8363–8384. <https://doi.org/10.1029/2018JD029576>.
- Kaimal, J.C., Finnigan, J.J., 1994. *Atmospheric Boundary Layer Flows: Their Structure and Measurement*. Oxford university press.
- Kaminski, T., Rayner, P.J., Heimann, M., Enting, I.G., 2001. On aggregation errors in atmospheric transport inversions. *J. Geophys. Res. Atmos.* 106 <https://doi.org/10.1029/2000JD900581>.
- Kanda, M., Inagaki, A., Miyamoto, T., Gryschka, M., Raasch, S., 2013. A new aerodynamic parametrization for real urban surfaces. *Bound.-Layer Meteorol.* 148, 357–377. <https://doi.org/10.1007/s10546-013-9818-x>.
- Kent, C.W., Grimmond, S., Barlow, J., Gatey, D., Kotthaus, S., Lindberg, F., Halios, C.H., 2017. Erratum to: evaluation of urban local-scale aerodynamic parameters: implications for the vertical profile of wind speed and for source areas (Boundary-Layer Meteorology, (2017), 164, 2, (183–213), 10.1007/s10546-017-0248-z). *Bound.-Layer Meteorol.* <https://doi.org/10.1007/s10546-017-0267-9>.
- Kljun, N., Calanca, P., Rotach, M.W., Schmid, H.P., 2015. A simple two-dimensional parameterisation for flux footprint prediction (FFP). *Geosci. Model Dev.* 8, 3695–3713. <https://doi.org/10.5194/gmd-8-3695-2015>.
- Knorr, W., Kattge, J., 2005. Inversion of terrestrial ecosystem model parameter values against eddy covariance measurements by Monte Carlo sampling. *Glob. Chang. Biol.* 11, 1333–1351. <https://doi.org/10.1111/j.1365-2486.2005.00977.x>.
- Koohkan, M.R., Bocquet, M., 2012. Accounting for representativeness errors in the inversion of atmospheric constituent emissions: application to the retrieval of regional carbon monoxide fluxes. *Tellus Ser. B Chem. Phys. Meteorol.* 64, 19047. <https://doi.org/10.3402/tellusb.v64i0.19047>.
- Kotthaus, S., Grimmond, C.S.B., 2012. Identification of Micro-scale anthropogenic CO₂, heat and moisture sources - processing eddy covariance fluxes for a dense urban environment. *Atmos. Environ.* 57, 301–316. <https://doi.org/10.1016/j.atmosenv.2012.04.024>.
- Kountouris, P., Gerbig, C., Totsche, K.U., Dolman, A.J., Meesters, A., A.G.C., Broquet, G., Maignan, F., Gioli, B., Montagnani, L., Helfter, C., 2015. An objective prior error quantification for regional atmospheric inverse applications. *Biogeosciences* 12, 7403–7421. <https://doi.org/10.5194/bg-12-7403-2015>.
- Kountouris, P., Gerbig, C., Rödenbeck, C., Karstens, U., Koch, T.F., Heimann, M., 2018. Atmospheric CO₂ inversions on the mesoscale using data-driven prior uncertainties: quantification of the European terrestrial CO₂ fluxes. *Atmos. Chem. Phys.* 18, 3047–3064. <https://doi.org/10.5194/acp-18-3047-2018>.
- Lauvaux, T., Schuh, A.E., Ullasz, M., Richardson, S., Miles, N., Andrews, A.E., Sweeney, C., Diaz, L.I., Martins, D., Shepson, P.B., Davis, K.J., 2012. Constraining the CO₂ budget of the corn belt: exploring uncertainties from the assumptions in a mesoscale inverse system. *Atmos. Chem. Phys.* 12, 337–354. <https://doi.org/10.5194/acp-12-337-2012>.
- Lauvaux, T., Miles, N.L., Deng, A., Richardson, S.J., Cambaliza, M.O., Davis, K.J., Gaudet, B., Gurney, K.R., Huang, J., O'Keefe, D., Song, Y., Karion, A., Oda, T., Patarasuk, R., Razlivanov, I., Sarmiento, D., Shepson, P., Sweeney, C., Turnbull, J., Wu, K., 2016. High-resolution atmospheric inversion of urban CO₂ emissions during the dormant season of the Indianapolis flux experiment (INFLUX). *J. Geophys. Res.* 121, 5213–5236. <https://doi.org/10.1002/2015JD024473>.
- Lauvaux, T., Gurney, K.R., Miles, N.L., Davis, K.J., Richardson, S.J., Deng, A., Nathan, B. J., Oda, T., Wang, J.A., Hutrya, L., Turnbull, J., 2020. Policy-relevant assessment of urban CO₂ emissions. *Environ. Sci. Technol.* 54, 10237–10245. <https://doi.org/10.1021/acs.est.0c00343>.
- Leclerc, M.Y., Foken, T., 2014. *Footprints in Micrometeorology and Ecology*, first ed. Springer, Dordrecht Heidelberg London New York.
- Levy, P., Drewer, J., Jammet, M., Leeson, S., Friborg, T., Skiba, U., van Oijen, M., 2020. Inference of spatial heterogeneity in surface fluxes from eddy covariance data: a case study from a subarctic mire ecosystem. *Agric. For. Meteorol.* 280 <https://doi.org/10.1016/j.agrformet.2019.107783>.
- Lian, J., Lauvaux, T., Utard, H., Bréon, F.M., Broquet, G., Ramonet, M., Laurent, O., Albarus, I., Cucchi, K., Ciais, P., 2022. Assessing the effectiveness of an urban CO₂ monitoring network over the Paris region through the COVID-19 lockdown natural experiment. *Environ. Sci. Technol.* 56, 2153–2162. <https://doi.org/10.1021/acs.est.1c04973>.
- Lietzke, B., Vogt, R., 2013. Variability of CO₂ concentrations and fluxes in and above an urban street canyon. *Atmos. Environ.* 74, 60–72. <https://doi.org/10.1016/j.atmosenv.2013.03.030>.
- Lietzke, B., Vogt, R., Feigenwinter, C., Parlow, E., 2015. On the controlling factors for the variability of carbon dioxide flux in a heterogeneous urban environment. *Int. J. Climatol.* 35, 3921–3941. <https://doi.org/10.1002/joc.4255>.
- Lindberg, F., Grimmond, C.S.B., Gabey, A., Huang, B., Kent, C.W., Sun, T., Theeuwes, N. E., Järvi, L., Ward, H.C., Capel-Timms, I., Chang, Y., Jonsson, P., Krave, N., Liu, D., Meyer, D., Olofson, K.F.G., Tan, J., Wästberg, D., Xue, L., Zhang, Z., 2018. Urban multi-scale environmental predictor (UMEP): an integrated tool for city-based climate services. *Environ. Model. Softw.* 99, 70–87. <https://doi.org/10.1016/j.envsoft.2019.09.020>.
- Liu, J.S., 2004. *Monte Carlo Strategies in Scientific Computing*, first ed. Springer Series in Statistics, New York.
- Macdonald, R.W., Griffiths, R.F., Hall, D.J., 1998. An improved method for the estimation of surface roughness of obstacle arrays. *Atmos. Environ.* 32, 1857–1864. [https://doi.org/10.1016/S1352-2310\(97\)00403-2](https://doi.org/10.1016/S1352-2310(97)00403-2).

- Matese, A., Gioli, B., Vaccari, F.P., Zaldei, A., Miglietta, F., 2009. Carbon dioxide emissions of the city center of Firenze, Italy: measurement, evaluation, and source partitioning. *J. Appl. Meteorol. Climatol.* 48, 1940–1947. <https://doi.org/10.1175/2009JAMC1945.1>.
- Mauder, M., Foken, T., 2004. Documentation and instruction manual of the eddy covariance software package TK2, Arbeitsgebn, Univ, Bayreuth, Abt. Mikrometeorol. <https://epub.uni-bayreuth.de/884/1/ARBERG026.pdf> (accessed 24 June 2022).
- McKain, K., Wofsy, S.C., Nehrkorn, T., Eluszkiewicz, J., Ehleringer, J.R., Stephens, B.B., 2012. Assessment of ground-based atmospheric observations for verification of greenhouse gas emissions from an urban region. *Proc. Natl. Acad. Sci. U. S. A.* 109, 8423–8428. <https://doi.org/10.1073/pnas.1116645109>.
- Menzer, O., McFadden, J.P., 2017. Statistical partitioning of a three-year time series of direct urban net CO₂ flux measurements into biogenic and anthropogenic components. *Atmos. Environ.* 170, 319–333. <https://doi.org/10.1016/j.atmosenv.2017.09.049>.
- Millward-Hopkins, J.T., Tomlin, A.S., Ma, L., Ingham, D., Pourkashanian, M., 2011. Estimating aerodynamic parameters of urban-like surfaces with heterogeneous building heights. *Bound.-Layer Meteorol.* 141, 443–465. <https://doi.org/10.1007/s10546-011-9640-2>.
- Minet, J., Laloy, E., Tychon, B., François, L., 2015. Bayesian inversions of a dynamic vegetation model at four European grassland sites. *Biogeosciences* 12, 2809–2829. <https://doi.org/10.5194/bg-12-2809-2015>.
- Moncrieff, J.B., Massheder, J.M., de Bruin, H., Elbers, J., Friborg, T., Heusinkveld, B., Kabat, P., Scott, S., Soegaard, H., Verhoef, A., 1997. A system to measure surface fluxes of momentum, sensible heat, water vapour and carbon dioxide. *J. Hydrol.* 188–189, 589–611. [https://doi.org/10.1016/S0022-1694\(96\)03194-0](https://doi.org/10.1016/S0022-1694(96)03194-0).
- Moncrieff, J.B., Clement, R., Finnigan, J., Meyers, T., 2004. Averaging, detrending and filtering of eddy covariance time series. In: Lee, X., Massman, W.J., Law, B.E. (Eds.), *Handbook of Micrometeorology: A Guide for Surface Flux Measurements*. Kluwer Academic, Dordrecht, pp. 7–31. https://doi.org/10.1007/1-4020-2265-4_2.
- Nathan, B.J., Lauvaux, T., Turnbull, J.C., Richardson, S.J., Miles, N.L., Gurney, K.R., 2018. Source sector attribution of CO₂ emissions using an urban CO/CO₂ Bayesian inversion system. *J. Geophys. Res. Atmos.* 123, 13,611–13,621. <https://doi.org/10.1029/2018JD029231>.
- Nemitz, E., Hargreaves, K.J., McDonald, A.G., Dorsey, J.R., Fowler, D., 2002. Micrometeorological measurements of the urban heat budget and CO₂ emissions on a city scale. *Environ. Sci. Technol.* 36, 3139–3146. <https://doi.org/10.1021/es010277e>.
- Nicolini, G., Antoniella, G., Carotenuto, F., Christen, A., Ciais, P., Feigenwinter, C., Gioli, B., Stagakis, S., Velasco, E., Vogt, R., Ward, H.C., Barlow, J., Chrysoulakis, N., Duce, P., Graus, M., Helfter, C., Heusinkveld, B., Järvi, L., Karl, T., Marras, S., Masson, V., Matthews, B., Meier, F., Nemitz, E., Sabbatini, S., Scherer, D., Schume, H., Sirca, C., Steeneveld, G.J., Vagnoli, C., Wang, Y., Zaldei, A., Zheng, B., Papale, D., 2022. Direct observations of CO₂ emission reductions due to COVID-19 lockdown across European urban districts. *Sci. Total Environ.* 830, 154662. <https://doi.org/10.1016/j.scitotenv.2022.154662>.
- Nieuwstadt, F.T.M., 1981. The steady-state height and resistance laws of the nocturnal boundary layer: theory compared with cabauw observations. *Bound.-Layer Meteorol.* 20, 3–17. <https://doi.org/10.1007/BF00119920>.
- Oke, T.R., Mills, G., Christen, A., Voegt, J.A., 2017. Urban climates. *Urban Clim.* <https://doi.org/10.1017/9781139016476>.
- Rannik, Ü., Vesala, T., Peltola, O., Novick, K.A., Aurela, M., Järvi, L., Montagnani, L., Mölder, M., Peichl, M., Pilegaard, K., Mammarella, I., 2020. Impact of coordinate rotation on eddy covariance fluxes at complex sites. *Agric. For. Meteorol.* 287. <https://doi.org/10.1016/j.agrformet.2020.107940>.
- Robert, C.P., Casella, G., 2004. *Monte Carlo Statistical Methods*, second ed. Springer Series in Statistics, New York.
- Roberts, G.O., Gelman, A., Gilks, W.R., 1997. Weak convergence and optimal scaling of random walk Metropolis algorithms. *Ann. Appl. Probab.* 7, 110–120. <https://doi.org/10.1214/aoap/1034625254>.
- Salgueiro, V., Cerqueira, M., Monteiro, A., Alves, C., Rafael, S., Borrego, C., Pio, C., 2020. Annual and seasonal variability of greenhouse gases fluxes over coastal urban and suburban areas in Portugal: measurements and source partitioning. *Atmos. Environ.* 223. <https://doi.org/10.1016/j.atmosenv.2019.117204>.
- Schmid, H.P., 2002. Footprint modeling for vegetation atmosphere exchange studies: a review and perspective. *Agric. For. Meteorol.* 113, 159–183. [https://doi.org/10.1016/S0168-1923\(02\)00107-7](https://doi.org/10.1016/S0168-1923(02)00107-7).
- Schmutz, M., Vogt, R., Feigenwinter, C., Parlow, E., 2016. Ten years of eddy covariance measurements in Basel, Switzerland: seasonal and interannual variabilities of urban CO₂ mole fraction and flux. *J. Geophys. Res.* 121, 8649–8667. <https://doi.org/10.1002/2016JD025063>.
- Stagakis, S., Chrysoulakis, N., Spyridakis, N., Feigenwinter, C., Vogt, R., 2019. Eddy covariance measurements and source partitioning of CO₂ emissions in an urban environment: application for Heraklion, Greece. *Atmos. Environ.* 201, 278–292. <https://doi.org/10.1016/j.atmosenv.2019.01.009>.
- Stagakis, S., Feigenwinter, C., Vogt, R., Kalberer, M., 2023. A high-resolution monitoring approach of urban CO₂ fluxes. Part 1 - bottom-up model development. *Sci. Total Environ.* 858, 160216. <https://doi.org/10.1016/j.scitotenv.2022.160216>.
- Stauf, J., Broquet, G., Bréon, F.M., Puygrenier, V., Chevallier, F., Xueref-Rémy, I., Dieudonné, E., Lopez, M., Schmidt, M., Ramonet, M., Perrussel, O., Lac, C., Wu, L., Ciais, P., 2016. The first 1-year-long estimate of the Paris region fossil fuel CO₂ emissions based on atmospheric inversion. *Atmos. Chem. Phys.* 16, 14703–14726. <https://doi.org/10.5194/acp-16-14703-2016>.
- Tarantola, A., 2005. *Inverse Problem Theory and Methods for Model Parameter Estimation*, 1st ed. Inverse Problem Theory and Methods for Model Parameter Estimation. Society for Industrial and Applied Mathematics (SIAM), Philadelphia, Pennsylvania, USA. <https://doi.org/10.1137/1.9780898717921>.
- UNFCCC, 2015. The Paris Agreement, COP 21, Paris, 12 December 2015. In: <https://unfccc.int/process-and-meetings/the-paris-agreement/the-paris-agreement> (accessed 24 June 2022).
- Velasco, E., Roth, M., Norford, L., Molina, L.T., 2016. Does urban vegetation enhance carbon sequestration? *Landsc. Urban Plan.* 148, 99–107. <https://doi.org/10.1016/j.landurbplan.2015.12.003>.
- Vesala, T., Kljun, N., Rannik, Ü., Rinne, J., Sogachev, A., Markkanen, T., Sabelfeld, K., Foken, T., Leclerc, M.Y., 2008. Flux and concentration footprint modelling: state of the art. *Environ. Pollut.* 152, 653–666. <https://doi.org/10.1016/j.envpol.2007.06.070>.
- Vickers, D., Mahrt, L., 1997. Quality control and flux sampling problems for tower and aircraft data. *J. Atmos. Ocean. Technol.* 14, 512–526. [https://doi.org/10.1175/1520-0426\(1997\)014<0512:QCAFS>2.0.CO;2](https://doi.org/10.1175/1520-0426(1997)014<0512:QCAFS>2.0.CO;2).
- Vogt, R., Christen, A., Rotach, M.W., Roth, M., Satyanarayana, A.N.V., 2006. Temporal dynamics of CO₂ fluxes and profiles over a central European city. *Theor. Appl. Climatol.* 84, 117–126. <https://doi.org/10.1007/s00704-005-0149-9>.
- Wagner, P.-R., Nagel, J., Marelli, S., Sudret, B., 2021. UQLab user manual – Bayesian inference for model calibration and inverse problems, report UQLab-V1.4-113, chair of risk, safety and uncertainty quantification, ETH Zurich, Switzerland. <https://www.uqlab.com/inversion-user-manual>.
- Webb, E.K., Pearman, G.I., Leuning, R., 1980. Correction of flux measurements for density effects due to heat and water vapour transfer. *Q. J. R. Meteorol. Soc.* 106, 85–100. <https://doi.org/10.1002/qj.49710644707>.
- WMO, 2022. IG3IS urban greenhouse gas emission observation and monitoring good research practice guidelines. https://library.wmo.int/doc_num.php?explnum_id=11292 (accessed 06 July 2023).
- Wu, L., Bocquet, M., Chevallier, F., Lauvaux, T., Davis, K., 2013. Hyperparameter estimation for uncertainty quantification in mesoscale carbon dioxide inversions. *Tellus Ser. B Chem. Phys. Meteorol.* 65, 20894. <https://doi.org/10.3402/tellusb.v65i0.20894>.
- Wu, L., Broquet, G., Ciais, P., Bellassen, V., Vogel, F., Chevallier, F., Xueref-Remy, I., Wang, Y., 2016. What would dense atmospheric observation networks bring to the quantification of city CO₂ emissions? *Atmos. Chem. Phys.* 16, 7743–7771. <https://doi.org/10.5194/acp-16-7743-2016>.
- Wu, K., Lauvaux, T., Davis, K.J., Deng, A., Coto, I.L., Gurney, K.R., Patarasuk, R., 2018. Joint inverse estimation of fossil fuel and biogenic CO₂ fluxes in an urban environment: an observing system simulation experiment to assess the impact of multiple uncertainties. *Elementa* 6. <https://doi.org/10.1525/elementa.138>.
- Wu, K., Davis, K.J., Miles, N.L., Richardson, S.J., Lauvaux, T., Sarmiento, D.P., Balashov, N.V., Keller, K., Turnbull, J., Gurney, K.R., Liang, J., Roest, G., 2022. Source decomposition of eddy-covariance CO₂ flux measurements for evaluating a high-resolution urban CO₂ emissions inventory. *Environ. Res. Lett.* 17, 074035. <https://doi.org/10.1088/1748-9326/ac7c29>.
- Xie, Z.T., Coceal, O., Castro, I.P., 2008. Large-Eddy simulation of flows over random urban-like obstacles. *Bound.-Layer Meteorol.* 129, 1–23. <https://doi.org/10.1007/s10546-008-9290-1>.
- Zilitinkevich, S.S., Tyuryakov, S.A., Troitskaya, Y.I., Mareev, E.A., 2012. Theoretical models of the height of the atmospheric boundary layer and turbulent entrainment at its upper boundary. *Izv. Atmos. Oceanic Phys.* 48, 133–142. <https://doi.org/10.1134/S0001433812010148>.